What Scalable Second-Order Information Knows for Pruning at Initialization

Ivo Gollini Navarrete*, Nicolás Mauricio Cuadrado Ávila, Martin Takáč & Samuel Horváth
Mohamed bin Zayed University of Artificial Intelligence
Abu Dhabi, UAE

Pruning remains an effective strategy for reducing both the costs and environmental impact associated with deploying large neural networks (NNs) while maintaining performance. Classical methods, such as OBD [1] and OBS [2], demonstrate that utilizing curvature information can significantly enhance the balance between network complexity and performance. However, the computation and storage of the Hessian matrix make it impractical for modern NNs, motivating the use of approximations. Recent research [3, 4] suggests that the top eigenvalues guide optimization in a small subspace, are identifiable early, and remain consistent during training. Motivated by these findings, we revisit pruning at initialization (PaI) to evaluate scalable, unbiased second-order approximations, such as the Empirical Fisher and Hutchinson diagonals. Our experiments show that these methods capture sufficient curvature information to improve the identification of critical parameters compared to first-order baselines, while maintaining linear complexity. Additionally, we empirically demonstrate that updating batch normalization statistics as a warmup phase improves the performance of data-dependent criteria and mitigates the issue of layer collapse. Notably, Hutchinson-based criteria consistently outperformed or matched existing PaI algorithms across various models (including VGG, ResNet, and ViT) and datasets (such as CIFAR-10/100, TinyImageNet, and ImageNet). Our findings suggest that scalable second-order approximations strike an effective balance between computational efficiency and accuracy, making them a valuable addition to the pruning toolkit. We make our code available [2].

1. Introduction

Advancements in computing and data availability have enabled large Neural Networks (NNs) to achieve exceptional progress in fields such as robotics [5], computer vision [6], and natural language processing [7]. However, the increasing size of these models raises concerns about computing costs and energy consumption [8], making them difficult to implement on edge devices or in resource-constrained settings [9]. In addition, large-scale training and inference have become another key focus area in climate change awareness [10, 11].

Model compression techniques, such as quantization [12], low-rank factorization [13], knowledge distillation [14], neural architecture search [15], and neural network pruning [1], aim to reduce model complexity while preserving performance. In particular, neural network pruning effectively decreases the model size and computational workload with minimal performance loss. Cheng et al. [9] classify pruning strategies based on three questions: (1) Is the acceleration universal or specific? (2) When does pruning occur in the training pipeline? (3) Is the pruning criterion predefined or learned during training?

Researchers mainly focus on pruning after training (PaT) because converged models produce more accurate estimates of parameter importance compared to randomly initialized ones [16]. Pruning criteria can range from simple random selection or parameter magnitude [8] to principled approaches that evaluate changes in loss [17]. Classical methods, such as Optimal Brain Damage

*Correspondence to ivo.navarrete@mbzuai.ac.ae
[2] https://github.com/Gollini/Scalable_Second_Order_PaI

Third Conference on Parsimony and Learning (CPAL 2026).

(OBD) [1] and Optimal Brain Surgery (OBS) [2], utilize curvature information to improve the balance between network complexity and performance. However, the large number of parameters in modern NNs makes the computation of the Hessian matrix infeasible, leading to the use of approximations [17].

The benefits of PaT come at the cost of training a dense model and subsequent parameter adjustments. This has sparked interest in Pruning at Initialization (PaI), which seeks to identify subnetworks before training to save computation. Frankle et al. [18] introduced the idea of "winning tickets," sparse subnetworks that can outperform dense models with the same initialization. However, finding these requires a computationally heavy prune-retrain strategy, prompting the search for more efficient algorithms [19, 20] and one-shot approaches to reduce overhead [21–23].

Incorporating second-derivative information directly at initialization seems to be a motivated step. However, there are reservations about relying on information from a randomly initialized model, given the high variance and the mismatch between the information of the early and converged curvature [24]. As a result, PaI research has favored zero and first-order methods. Nevertheless, the findings of Gur et al. [3] show that gradient descent rapidly concentrates in a tiny subspace dominated by the top eigenvectors and is preserved throughout training. Furthermore, Karakida et al. [4] analyzed the spectrum of the Fisher Information Matrix (FIM) at initialization. They determined that for randomly initialized wide networks, the local geometry is dominated by a small number of directions. Together, these results suggest that even at initialization, curvature information already identifies important directions to preserve during training.

To validate our assumptions, we conducted a small-scale experiment using two classes from the MNIST dataset [25]. At the beginning of the experiment, we computed the Hessian and obtained its eigendecomposition, $H_0 = U_0 \Sigma_0 U_0^T$, where Σ is the diagonal matrix of eigenvalues and U is the orthogonal matrix of corresponding eigenvectors. We then measured the movement of the parameters from initialization to the end of training ($\Delta w = w_0 - w_t$). As shown in Figure 1, projecting this displacement onto the Hessian eigenbasis, denoted as $proj = |U_0^T \Delta w|$, indicates that the largest movements in parameter space relate to the directions associated with the largest magnitude eigenvalues $|\lambda|$ of H_0. A detailed description of the experimental setup and results is provided in Appendix A, where the reader can observe that this trend emerges after the first optimization step and is maintained throughout the training process.

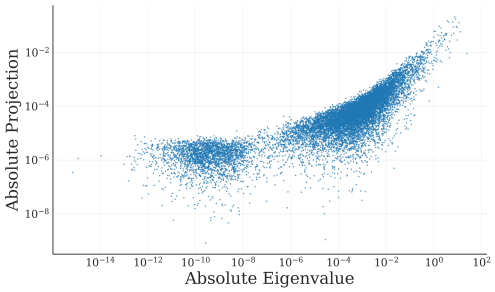

Figure 1: Relationship between curvature and parameter displacement. Each point corresponds to one eigendirection of the Hessian calculated at initialization.

Motivated by these findings, we revisit the one-shot PaI setting and examine scalable estimators of the Hessian matrix for pruning. Specifically, we evaluate unbiased estimators of the Hessian diagonal, such as the Empirical FIM diagonal and Hutchinson's estimator diagonal, effectively reducing the computation overhead of second-order methods from quadratic to linear [26].

We also propose a method to alleviate *layer collapse*, a failure mode in *data-dependent* methods that disrupts information flow between layers due to bottlenecks or complete removal of a layer [23]. Gradient-based PaI methods often assign disproportionately low scores to wide layers, pruning them first, and making the model untrainable [16]. We show that a simple warmup phase to update batch normalization statistics yields more reliable gradient estimates and effectively mitigates layer collapse.

Our experiments used CIFAR-10/100, TinyImageNet, and ImageNet on a range of models (VGG, ResNet, and ViT). Our results show that coarse second-order information consistently improves pruning outcomes compared to long-standing one-shot pruning baselines. Moreover, the proposed warmup phase reduced the effect of layer collapse and improved the performance of data-dependent methods. Notably, the Hutchinson diagonal approximation with warmup surpasses magnitude-based PaT in extreme sparsities ($\geq 90\%$), a long-standing barrier for PaI methods [27].

Our key contributions are summarized as follows: (1) We revisit one-shot PaI with scalable second-order approximations for a balance between performance and computation overhead. (2) Our experiments show that coarse curvature information outperforms long-standing PaI one-shot baselines. (3) We show that updating batch normalization statistics provides a simple and effective fix to layer collapse and improves the performance of data-dependent criteria. And (4) We empirically demonstrate that principled pruning methods narrow the gap between PaI and PaT.

2. Background & Related Work

Problem Definition. Given access to the training set $\mathcal{D} = \{(x_n, y_n)\}_{n=1}^{N}$, composed of tuples of input $x_n \in \mathcal{X}$ and output $y_n \in \mathcal{Y}$, the goal is to learn a model parameterized by $w \in \mathbb{R}^d$ that maps $f : \mathcal{X} \to \mathcal{Y}$ by minimizing the objective function:

$$\mathcal{L}(w) = \frac{1}{N} \sum_{n=1}^{N} l(y_n, f(x_n; w)). \tag{1}$$

We denote $q \in \mathcal{Q}$, with $\mathcal{Q} = \{1, 2, \ldots, d\}$, as an index to refer to an element w_q in the parameter vector w.

The Hessian Matrix. Consider the scalar-valued function (1) is twice differentiable. We refer to the matrix of second partial derivatives as the Hessian:

$$H(w) := \nabla^2 \mathcal{L}(w) \in \mathbb{R}^{d \times d}. \tag{2}$$

It captures the local curvature of the loss landscape around w, indicating how rapidly the gradient changes in different directions. Direct computation and storage of the entire matrix requires $\mathcal{O}(d^2)$ time and memory, infeasible for modern networks. Consequently, many second-order methods rely on approximations, especially in optimization research. Hessian-free methods exploit the Hessian-vector product (HVP) but require many iterations or additional techniques to achieve stability [28, 29]. Other approaches, such as the Generalized Gauss-Newton (GGN) [30], approximate layer-wise blocks to approximate only parts of the Hessian. The Kronecker-factored Approximate Curvature method (KFAC) reduces the GGN calculation of each block by writing it as a product of two smaller matrices [31]. However, storing KFAC matrices can become prohibitively expensive for large models.

A scalable alternative is to approximate only the Hessian's diagonal. Although the exact calculation of the Hessian diagonal remains quadratic, stochastic methods yield unbiased estimates [32]. For example, Curvature Propagation (CP) [33] provides such an estimator at the cost of two gradient evaluations. More recently, Yao et al. [26] used Hutchinson's estimator to approximate $\mathrm{diag}(H)$ through randomized probes z drawn from a Rademacher distribution.

The Fisher Information Matrix (FIM). The FIM has been used as an approximation of the Hessian to increase computational speed [34]. It is defined as the expectation of the second moment of the score function. Based on the probabilistic concept that minimizing the loss function $l(y, f(x; w))$ is equivalent to maximizing the negative log-likelihood $-\log p(y \mid x, w)$, we can express the FIM in terms of the Hessian under regularity conditions [35]:

$$F(w) = -\mathbb{E}\left[\nabla^2 \log p(y \mid x, w)\right] = \mathbb{E}\left[\nabla^2 l(y, f(x; w))\right]. \tag{3}$$

The FIM approximation reduces computational demands, but still requires $\mathcal{O}(d^2)$ memory. Soen et al. [36] discussed the trade-offs of using only the diagonal of the FIM, which reduces the complexity to $\mathcal{O}(d)$. In practice, the FIM diagonal is estimated from the empirical training distribution, providing an unbiased plug-in estimator that retains essential geometric information. This leads to the following formulation:

$$\mathrm{diag}(\hat{F}) = \frac{1}{N} \sum_{n=1}^{N} \nabla l(y_n, f(x_n; w))^2. \tag{4}$$

This approximation can be intuitively understood as follows: Each entry in $\mathrm{diag}(\hat{F})$ is the average of the squared gradient of the model's output with respect to a parameter. Larger entries indicate parameters that have a greater influence on the model's output.

PaT Methods. Early pruning focused on removing parameters with low performance impact (low saliency). First, Hanson et al. [37] found that parameters with larger magnitudes are generally more significant. Then, LeCun et al. [1] introduced OBD, a more principled saliency measure that uses a second-order Taylor series to assess the effect of removing parameters under three assumptions: (1) the Hessian matrix is approximated using only its diagonal, (2) the first-order term of the Taylor series is negligible for a converged model, and (3) the local loss model is assumed to be quadratic, discarding higher-order terms. The saliency of the parameter w_q is defined as:

$$s_q = \frac{1}{2} w_q^2 H_{qq}, \tag{5}$$

A few years later, Hassibi et al. [2] presented OBS, highlighting the importance of a more comprehensive representation of second-order information, which includes off-diagonal elements, and criticized the need to fine-tune the subnetwork. They derived a general expression for saliency that includes (5) as a special case, and an expression to recalculate the magnitude of all parameters after removing a parameter w_q:

$$s_q = \frac{w_q^2}{2[H^{-1}]_{qq}}, \qquad \delta w = -\frac{w_q H^{-1} e_q}{[H^{-1}]_{qq}}. \tag{6}$$

More recently, Theis et al. [38] adapted OBD to the size of current models by approximating the Hessian diagonal using the empirical FIM diagonal. As in (5), the first term of the Taylor expansion vanishes, yielding the saliency metric Fisher Pruning (FP):

$$s_q = \frac{1}{2} w_q^2 \hat{F}_{qq}. \tag{7}$$

Extending FP to structured pruning, Liu et al. [39] employed Fisher information to estimate the importance of channels identified by a layer grouping algorithm that exploits the network's computation graph. Singh et al. [17] adapted OBS to modern times using an iterative, blockwise method to approximate the inverse Hessian. The authors demonstrated the relationship between the empirical FIM inverse $\hat{F}^{-1}$ and the Hessian inverse H^{-1}, concluding that the former is a good approximation of the latter as long as the application is scale-invariant.

PaI Methods. When referring to methods that prune at initialization time, it is necessary to mention the *Lottery Ticket Hypothesis* introduced by Frankle et al. [18]. Certain initializations can reveal smaller subnetworks that match or surpass the performance of the original dense network. Their iterative pruning approach identified performant subnetworks in ResNet18 and VGG19 with compression rates of $80 - 90\%$ for the CIFAR-10 classification task. However, they required a computationally expensive process, opening the question: If winning tickets exist, can we find them inexpensively?

Lee et al. [21] addressed this question with SNIP, a single-shot pruning method that measures *connection sensitivity*. They introduce an auxiliary indicator vector $c \in \{0, 1\}^d$ that specifies whether a connection is active with a Hadamard product $c \odot w$. From this perspective, the effect of removing the connection q on the loss is approximated as a directional derivative $g_q(w; \mathcal{D})$ with respect to c_q:

$$\Delta\mathcal{L}_q(w) = \lim_{\epsilon \to 0} \frac{\mathcal{L}(c \odot w) - \mathcal{L}((c - \epsilon e_q) \odot w)}{\epsilon}\Big|_{c=\mathbb{1}} = w_q \frac{\partial \mathcal{L}(w)}{\partial c_q} = g_q(w). \tag{8}$$

This method can be intuitively understood as follows: The magnitude of the gradient with respect to c indicates how each connection affects the loss, regardless of the direction. Their final sensitivity is defined as:

$$s_q = \frac{|g_q(c \odot w)|}{\sum_{k=1}^{m} |g_k(c \odot w)|}. \tag{9}$$

Wang et al. [22] proposed Gradient Signal Preservation (GraSP), a method based on the concept of neural tangent kernel (NTK) [40], under the premise that effective training requires preserving gradient flow through the model. GraSP selects parameters that encourage the NTK to be large in the direction of the gradients in the output space. They derived a sensitivity metric that measures the response to a stimulus δ:

$$S(\delta) = \Delta\mathcal{L}(w_0 + \delta) - \Delta\mathcal{L}(w_0) = 2\delta^\top H \nabla\mathcal{L}(w) + \mathcal{O}(||\delta||_2^2). \tag{10}$$

Tanaka et al. [23] proposed SynFlow, a data-agnostic pruning method that identifies sparse, trainable subnetworks at initialization. Unlike data-dependent methods, which can induce *layer collapse* by removing entire layers, SynFlow iteratively preserves the total "synaptic flow," i.e., the cumulative strength of connections, thereby maintaining information flow and network trainability.

3. Methodology

Setting Definition. Following the taxonomy in [41], the main setting focuses on unstructured pruning. A binary mask $m \in \{0,1\}^d$ is applied to induce sparsity, effectively reducing the parameter count of the model. We construct m using an importance criterion and the target sparsity level. The pruned model is defined as $f(x_n; m \odot w)$, where $\odot$ denotes the Hadamard product between m and the model weights w. The objective (1) then becomes:

$$\mathcal{L}(m \odot w) = \frac{1}{N} \sum_{n=1}^{N} l(y_n, f(x_n; m \odot w)). \tag{11}$$

Sensitivity Score. Following OBD [1], we start by approximating the objective (1) using a Taylor series. The perturbation δw of the parameter vector will change $\mathcal{L}$ by

$$\delta\mathcal{L} = \mathcal{L}(w) - \mathcal{L}(w + \delta w) = \delta w^T \nabla\mathcal{L}(w) + \frac{1}{2}\delta w^T H \delta w + \mathcal{O}(||\delta w||^3). \tag{12}$$

Unlike OBD, the gradients are far from zero in the PaI setting, and neglecting the first-order term is not viable. Still, we assume the local error is quadratic and discard higher-order components. This approach assumes that individually deleting the parameters yields the same perturbation as removing them simultaneously. We aim to maintain a linear complexity of $O(d)$ to make the sensitivity score practical and minimize computational overhead. Therefore, we restrict the computation of the Hessian to diagonal approximations that capture enough curvature information. Then, (12) becomes:

$$\delta\mathcal{L} = \sum_{q \in \mathcal{Q}} \delta w_q \frac{\partial\mathcal{L}(w)}{\partial w_q} + \frac{1}{2} \sum_{q \in \mathcal{Q}} \delta w_q^2 H_{qq}. \tag{13}$$

As explained in [21], induced perturbations at initialization will cause $\mathcal{L}$ to increase, decrease, or remain the same. Changes of high magnitude to (13) (positive or negative) mean that the objective function is significantly *sensitive* to the parameters q and should be preserved for the pruned model to learn. We define the sensitivity of the parameter w_q as follows:

$$s_q = \left| w_q \frac{\partial\mathcal{L}(w)}{\partial w_q} + \frac{1}{2} w_q^2 H_{qq} \right|. \tag{14}$$

Scalable Hessian approximations. Firstly, we consider the Hutchinson approximation employed by AdaHessian [26]. We sample a random Rademacher vector $z \in \{-1, 1\}^d$ and compute the HVP Hz. In practice, the HVP is computed via a single backpropagation trick, thereby keeping the cost on the order of a gradient pass. The elementwise product of Hz and z, averaged over random draws, yields an unbiased estimator of the Hessian diagonal:

$$\mathrm{diag}(\hat{H}) = \mathbb{E}_z\big[(Hz) \odot z\big]. \tag{15}$$

With the incorporation of $\mathrm{diag}(\hat{H})$ into (14), we define Hutchinson-Taylor Sensitivity (HTS) as our first parameter importance score:

$$s_q = \left| w_q \frac{\partial\mathcal{L}(w)}{\partial w_q} + \frac{1}{2} w_q^2 \hat{H}_{qq} \right|. \tag{16}$$

Secondly, the equivalence between FIM and Hessian described in (3) only holds in convergence when the parameter vector w maximizes the likelihood $\mathbb{E}[\nabla \log p(y \mid x, w)] = 0$. However, Karikada et al. [4] showed that even at initialization, the FIM captures essential geometric properties of the parameter space. Some FIM eigenvalues are close to zero and indicate local flatness, while others are significantly large and induce substantial distortions in specific directions. We test whether the signals from the empirical FIM diagonal are strong enough to identify important parameters. In addition, the FIM has the desirable property of being PSD by construction, ensuring a stable representation. We define Fisher-Taylor Sensitivity (FTS) incorporating $\mathrm{diag}(\hat{F})$ into (14):

$$s_q = \left| w_q \frac{\partial\mathcal{L}(w)}{\partial w_q} + \frac{1}{2} w_q^2 \hat{F}_{qq} \right|. \tag{17}$$

Baselines comparison and Taylor Series Ablation. For comparison, we evaluate our proposed criteria against the following pruning methods: random, parameter magnitude, gradient norm (GN), SNIP [21], GraSP [22], and SynFlow [23]. Additionally, we decompose the terms in (14) to gain a better understanding of the Taylor expansion. We do not isolate the first-order component since Wang et al. [22] show that SNIP is equivalent to computing its absolute value:

$$s_q = \left| w_q \frac{\partial \mathcal{L}(w)}{\partial w_q} \right|.$$

For the second-order component, we extract two extra sensitivity criteria. First, we directly evaluate the diagonal approximations of the Hessian, referring to them as Hutchinson Diagonal (HD) and Fisher Diagonal (FD):

$$s_q = \hat{H}_{qq}, \qquad s_q = \hat{F}_{qq}. \tag{18}$$

Second, we evaluate the effect of using only the second-order term as in OBD [1] or Fisher Pruning [38], referring to them as Hutchinson Pruning (HP) and Fisher Pruning (FP):

$$s_q = w_q^2 \hat{H}_{qq}, \qquad s_q = w_q^2 \hat{F}_{qq}. \tag{19}$$

Pruning Mask. Given a data set partition, we compute the vector s that contains the sensitivity scores s_q for each parameter w_q. We generate the saliency scores using a subset of the training set as in [27]. To create the pruning mask m, we define a percentile p to narrow the subset containing the parameter index to retain:

$$\mathcal{R} = \{q \mid s_q \text{ is in the top } (1-p) \text{ of scores}\}.$$

Using this subset $\mathcal{R}$, the elements of the binary mask m are defined using the following rule: $m_q = 1$ if $q \in \mathcal{R}$ and $m_q = 0$ otherwise. We produce the pruned model $f(x; m \odot w_0)$ with the Hadamard product between the binary mask m and the vector of the initial parameters of the model w_0, with the sparsity ratio defined as:

$$\text{sparsity} = \tfrac{1}{d} \textstyle\sum_q m_q,$$

where d is the total number of parameters of the dense model. Once the mask is applied, the pruned model is optimized utilizing stochastic gradient descent to minimize the objective function (11). It is important to note that our pruning setting excludes parameters from batch normalization and the output layers, as we consider them crucial for enabling learning and performing the designed task. We also skip bias parameters, since they are initialized to zero and would be pruned immediately.

4. Results and Discussion

We progressively evaluate the effectiveness of the presented pruning criteria by increasing model and task complexities in various setups using benchmarks commonly employed in the unstructured pruning literature [27]: CIFAR-10/100 [42], TinyImageNet [43], and ImageNet-1K [43] datasets in ResNet [44] and VGG [45] architectures (training details in Appendix B). Additionally, we evaluated the performance of our proposed criteria in a pre-finetuning structured pruning setup for the visual transformer ViT-B/16 [46]. We report all metrics across three random seeds.

Computational Complexity. First, we compare the pruning criteria by complexity. Table A2 (Appendix C) details the practical and theoretical time and space complexities. The proposed diagonal estimations reduce the complexity of the Hessian matrix to $\mathcal{O}(d)$, and reduce the computational cost to just $\mathcal{O}(Nd)$, the same as first-order methods such as SNIP or GN.

Base Reference Case. We define CIFAR-10 classification using ResNet18 as our base reference case. Random pruning is performant in the low-sparsity regime and is the first baseline any proposed method should surpass. As seen in Figure 2a and Table A7 (Appendix G.1), random's performance is comparable to the rest of the methods up to 60% sparsity. Therefore, our analysis focuses on the high sparsity regime ($\geq 80\%$), where the differences and limitations of the methods are most pronounced.

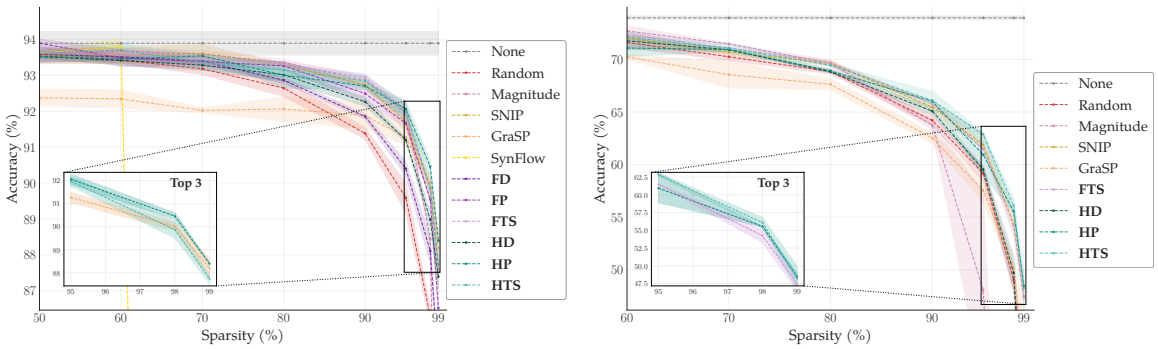

(a) ResNet-18/CIFAR-10 without warmup.

(b) ResNet-50/Imagenet-1K without warmup.

Figure 2: Test accuracy across sparsity levels under various PaI methods for our base reference case of CIFAR-10 with ResNet-18 on the left, and the more complex Imagenet-1K with ResNet-50 on the right. The dashed gray line denotes the baseline accuracy without pruning.

Magnitude pruning is the second baseline to surpass, as it is the most widely studied method in the literature. It performs well for moderate sparsities (up to 80%), but its performance decays rapidly as the sparsity increases. We observe a similar behavior for GN, SNIP, and GraSP, but with a slower decay, surpassing both baselines. The data-agnostic method SynFlow struggles to pass from moderate sparsities, after which a sudden drop of performance is observed[3]. We highlight that across the sparsity range, Hutchinson-based criteria are top-performers or matching metrics. Most importantly, HP dominates the high-sparsity regime, suggesting that even coarse second derivative information improves the trade-off between model complexity and performance in PaI.

We refer the reader to the Appendix D for a sensitivity analysis on the number of samples per class used to estimate parameter importance scores. The Hutchinson-based criteria are robust, with no significant difference between using a single sample per class and the full training set for score computation, further solidifying the value of second-order information. On the other hand, the remaining methods show a slight decrease in performance as the number of samples increases, with FD being most affected. As a general recommendation for the PaI setting, the practitioner should increase the batch size for score computation when using large subsets, as this accelerates computation time and prevents the performance drop observed in FD. Appendix E discusses the ranking stability robustness when using different numbers of Rademacher probes to compute the Hutchinson diagonal approximation.

Increasing Model Complexity. We evaluated the consistency of our results by replacing the model in our reference case with ResNet-50 (Table A11 in Appendix G.3), a deeper and wider architecture commonly used in large-scale vision tasks. Similarly, the performance of random pruning is comparable to the 93.17 baseline accuracy up to 70% sparsity. Magnitude pruning suffered from layer collapse as the model size increased. GN, SNIP, and GraSP showed a behavior consistent with the base case. SynFlow is the best-performing model at low sparsities, but the same failure mode occurs as sparsity increases. The HP and FTS criteria consistently appear among the top performers at high sparsity. Results continue to support the relevance of second-order information.

Increasing Task Complexity. We increase the difficulty of the classification task by evaluating the CIFAR-100 and TinyImageNet datasets with ResNet-18. We observe the same trends, with the HP criterion notoriously outperforming in the high sparsity regime on both datasets as shown in Figure A4 and Table A12 (Appendix H.1) for CIFAR-100, and Figure A5 and Table A16 (Appendix I.1) for TinyImageNet. We highlight that the advantage of Hutchinson-based criteria becomes more noticeable as the task complexity increases. For CIFAR-100, HP's accuracy performance at the highest sparsity improves by ~ 2 points relative to the closest non-Hutchinson method. For TinyImageNet, the same gap at the highest sparsity increases by ~ 3 points.

[3]Reported issues in the repository of the original SynFlow implementation highlight inconsistencies due to zero gradients that prune whole layers.

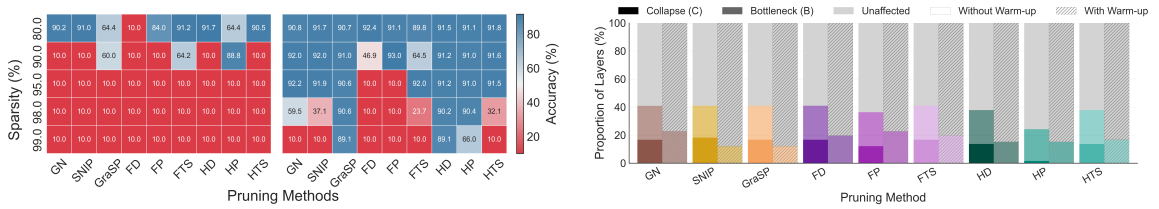

(a) (b)

Figure 3: (**a**) Effect of a warmup phase on training stability in CIFAR-10 with VGG-19 at extreme sparsity ratios. Several methods exhibit systematic layer collapse without a warmup (left), leading to near-random performance. A warmup phase (right) largely prevents collapse and preserves accuracy across methods. (**b**) Importance of batch normalization statistics (BNS) update to prevent layer collapse. We studied the case of VGG-19 pruning at 95% sparsity.

Increasing Model and Task Complexity. Finally, for the last set of experiments in the unstructured PaI setting, we increased the complexity by evaluating ImageNet-1K with ResNet-50, resulting in a significant increase in the number of classes. As seen in Figure 2b and Table A18 (Appendix J), HTS and HP are the constant top-performers across the evaluated sparsities.

Consolidated Analysis. We empirically showed that Hutchinson's diagonal approximation improves the trade-off between sparsity and performance at initialization. While the theoretical motivation for the Taylor expansion suggests the inclusion of first-order terms (HTS/FTS), the empirical strength of HP suggests that the high variance and poor alignment of gradients at initialization might destabilize the first-order contribution. Also, Fisher-based criteria lagged behind Hutchinson variants. The reliance on solely first-order statistics, as defined in Equation (4), suggests the FIM diagonal variants might be better suited for later stages of training. For example, near convergence, where both the FIM and the Hessian often become diagonal dominant [17], and the FIM more closely approximates the Hessian, formalized in Equation (3). Regardless, our results align with the observations of Yvinec et al. [47], which indicated that magnitude-based pruning may remove low-magnitude parameters that contribute to performance. In Appendix M, we illustrate the difference in parameter selection between magnitude-based and principled approaches, showing how magnitude might not be the best indication of importance.

Preventing Layer Collapse. Table A9 (Appendix G.2) and Table A14 (Appendix H.2) show the performance of different pruning criteria evaluated in CIFAR-10 and CIFAR-100, respectively, with VGG-19. All data-dependent methods suffer a drastic performance drop at higher sparsities. This behavior is consistent with the *layer collapse* phenomenon described by Tanaka et al. [23], in which pruning removes entire layers (or most of their parameters), disrupting information flow and rendering the model untrainable. We propose updating the batch normalization statistics as a warmup phase before forming the pruning mask.

Figure 3a illustrates how our proposed warmup step can mitigate layer collapse. Notably, the methods that can mitigate layer collapse up to the highest sparsity rely solely on second-order information (GraSP, HD, HP), further supporting the interpretation that second-order signals prove a more stable criterion in the PaI setting. Figure 3b presents a visual representation of the results in Table A6 (Appendix F). It is clearly observed that at a 95% sparsity level, updating the batch-norm statistics reduces the number of collapsed layers to 0% and significantly reduces the percentage of bottlenecks, enabling the training of the pruned model. We refer the reader to Tables A10 (Appendix G.2) and Table A15 (Appendix H.2) for detailed results on CIFAR-10 and CIFAR-100, respectively.

Improving Gradient Estimation. We further analyze the effect of the warmup step using ResNet-18 with CIFAR-10 (Table A8 in Appendix G.1), CIFAR-100 (Table A13 in Appendix H.1) and Tiny-ImageNet (Table A17 in Appendix I.1). We observe a constant improvement across all gradient-dependent methods. In particular, the HD criterion significantly improves the estimation of the Hessian diagonal, becoming the top performer across the three experiments. For the base reference case, performance increased by 1.57, 2.39, and 1.96 for sparsity ratios 95%, 98%, and 99%, respectively. This simple yet effective step not only mitigates the effect of layer collapse but also enables more accurate gradient estimation at initialization.

PaI vs. PaT comparison. Frankle et al. [27] strongly criticized PaI methodologies for consistently underperforming compared to magnitude-based PaT. However, their analysis did not assess how the PaI-designed criteria perform in the post-training setting. Table A19 (Appendix K.1) evaluates all criteria in the base reference case under the same PaT retraining protocol as [27]. Our results show that principled criteria outperform magnitude also in the PaT setting, with HP consistently ranking among the top performers. Notably, FIM-based variants significantly improve in the PaT setting and even match Hutchinson-based criteria, aligning with our interpretation that the FIM diagonal limits in the PaI setting are not intrinsic to the method but rather stage-dependent.

In Table A20 (Appendix K.1), we compute the performance gain of the metrics in the PaT setting over the PaI setting with warmup for data-dependent methods. GN and FD are the methods that benefit the most from the PaT setting, given the complete overcoming of layer collapse at high sparsities. Nevertheless, as we increase the sparsity, it becomes clear that the advantage of magnitude-based PaT over PaI methodologies stems from training a fully dense model rather than from the method's inherent strength. For example, the performance gain of magnitude PaT over its PaI counterpart at 99% sparsity is greater than 12 points, whereas for principled methods it is only around 1 point. As previously stated, the warmup phase significantly improves the HD criterion, enabling the PaI method to slightly outperform its own PaT counterpart at the highest sparsities and even exceed the performance of magnitude-based PaT. These results solidify the value of scalable second-order information and provide insights into potentially breaking the long-standing wall for PaI methods without training a fully dense model.

Structured pruning of Transformers. Transformers exhibit strong inter-parameter dependencies due to the structural redundancies of their components, such as multi-head attention and residual connections. Unstructured pruning removes individual weights without accounting for these interactions, which can disrupt key pathways and degrade performance unless carefully compensated for during training or fine-tuning [9]. Furthermore, in practice, unstructured pruning rarely leads to meaningful reductions in FLOPs or wall-clock inference time without specialized kernels or hardware. These observations suggest that structured pruning targeting entire attention heads, blocks, or projection subspaces can better respect the transformer's computational topology and produce more stable efficiency–performance trade-offs. Although our work focuses on unstructured PaI, it is valuable to test whether our proposed pruning metrics can remain informative in a structured PaI setting where decisions operate over larger, computationally meaningful units rather than individual weights.

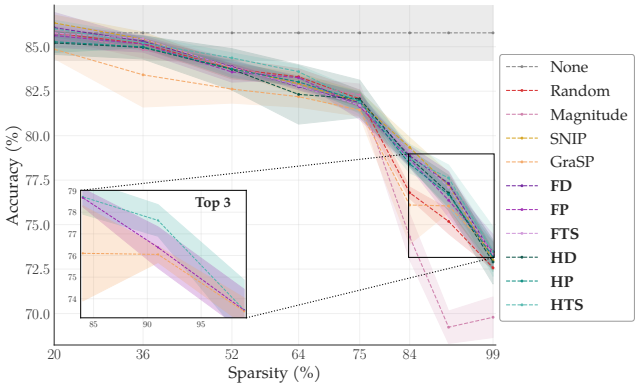

Figure 4: Structured pruning of ViT-B/16 in CIFAR-10: Test accuracy across sparsities for all the importance-based metrics.

Pre-Finetune Pruning Setup Transformers are known to be data-hungry, and it is hard to achieve state-of-the-art performance training from scratch. Therefore, we follow the same protocol as Dosovitskiy et al. [46] to define a pre-finetune pruning setting for our transformer experiments (details in Appendix L). Specifically, we evaluated CIFAR-10 with ViT-B/16 (5.61 billion parameters) pretrained on a different distribution dataset (ImageNet-1K). Following Sun et al. [48], we used the library torch-pruning[4] for structured pruning of PyTorch models. We employ per-layer structured pruning, ensuring that pruning decisions adhere to layer-wise constraints and avoid invalid graph states.

[4]https://github.com/VainF/Torch-Pruning

Table 1: Results of structured pruning for high and extreme sparsities: we used different criteria to perform per-layer pruning for the model ViT-B/16 in the CIFAR-10 dataset. Bold values indicate the best average performance among three random seeds. Baseline accuracy (no pruning): 85.78 $\pm$ 1.56.

Sparsity (%)	FLOPs	Runtime (min)	Random	Magnitude	SNIP	GraSP	FD	FP	FTS	HD	HP	HTS
75	1.40G	22	82.07 $\pm$ 0.50	**82.29 $\pm$ 0.61**	81.89 $\pm$ 0.57	81.44 $\pm$ 0.35	81.86 $\pm$ 0.17	81.64 $\pm$ 0.73	81.70 $\pm$ 0.59	82.07 $\pm$ 1.05	81.95 $\pm$ 0.51	81.88 $\pm$ 0.65
84	0.90G	18	76.79 $\pm$ 0.32	74.31 $\pm$ 1.28	**79.34 $\pm$ 0.55**	76.10 $\pm$ 2.20	78.87 $\pm$ 0.56	78.67 $\pm$ 0.42	79.15 $\pm$ 0.24	78.76 $\pm$ 0.43	78.41 $\pm$ 0.20	78.71 $\pm$ 0.80
91	0.50G	13	75.18 $\pm$ 0.69	69.23 $\pm$ 0.91	77.20 $\pm$ 0.73	76.05 $\pm$ 0.37	77.31 $\pm$ 0.67	76.37 $\pm$ 0.95	77.10 $\pm$ 0.89	76.78 $\pm$ 0.99	76.69 $\pm$ 0.70	**77.62 $\pm$ 0.73**
99	0.06G	10	72.57 $\pm$ 0.08	69.79 $\pm$ 1.14	73.00 $\pm$ 0.57	73.42 $\pm$ 0.62	73.28 $\pm$ 0.24	73.47 $\pm$ 0.97	73.32 $\pm$ 0.74	72.90 $\pm$ 1.24	73.18 $\pm$ 0.82	**73.48 $\pm$ 1.39**

Structured Pruning Analysis. As seen in Figure 4, at low and moderate sparsity levels, most criteria perform similarly, suggesting that structured decisions are relatively trivial in this regime. As we increase target sparsity, first- and second-order criteria exhibit greater robustness to degradation, consistently achieving higher accuracy. We highlight that, although the performances in our experiment remain very comparable, Hutchinson-based methods consistently yield a higher average accuracy for most evaluated sparsity levels. This further solidifies the idea that second-order information at initialization remains relevant even for structured PaI. Table 1 also shows that as sparsity increases, the model's size, FLOPs, and runtime are drastically reduced. Our general results show the value of principled methods for unstructured pruning and how they translate into practical approaches for structured pruning.

5. Limitations

(1) The verification of the findings described in [3] was performed in a relatively easy small-scale setting. As complexity increases, experiments become computationally infeasible to validate and may become unreliable. We consider the extended analysis of this phenomenon an interesting research direction for future work. (2) We operate under the assumption that the FIM and Hutchinson diagonals are good enough approximations of second-order information at initialization. The diagonal approximation assumes that parameters are non-interacting at the second-order level. Future work should expand to better approximations of the Hessian, even if the computational cost is no longer linear. (3) The proposed warmup step can be applied only to architectures with batch normalization layers. While batch normalization layers are integrated into most modern architectures, future research can explore alternatives for architectures that don't incorporate this type of layer.

6. Conclusion

In this work, we validate the assumption that second-order information provides valuable information from a random initialization in a small-scale experiment. Then, we proposed a suite of one-shot PaI methods based on scalable diagonal approximations of second-order information. We show the effectiveness of approximations in both structured PaI and PaT settings, especially in the extreme sparsity regime. The results show that Hutchinson variants consistently outperform or match the SOTA PaI methods across different models, task complexities, and sparsities. Additionally, we show that a warmup phase to update batch normalization statistics mitigates layer collapse when using data-dependent methods and enhances the performance of the Hutchinson estimator. We demonstrate that even coarse second-order methods can reduce the performance gap between PaI and PaT, providing a step toward more efficient and theoretically grounded model compression techniques. We also demonstrated that principled methods are relevant to pruning transformers in the structured PaI setting. Our general results reinforce the idea that there is no silver bullet for pruning and that the criteria are complementary. Still, we demonstrate that scalable second-order approximations strike an effective balance between computational efficiency and accuracy, making them a valuable addition to the pruning toolkit. Future work includes refining the approximations to capture off-diagonal interactions and exploring integration with other compression techniques, such as quantization.

References

[1] Yann LeCun, John Denker, and Sara Solla. Optimal brain damage. *Advances in neural information processing systems*, 2, 1989.

[2] Babak Hassibi and David Stork. Second order derivatives for network pruning: Optimal brain surgeon. *Advances in neural information processing systems*, 5, 1992.

[3] Guy Gur-Ari, Daniel A Roberts, and Ethan Dyer. Gradient descent happens in a tiny subspace. *arXiv preprint arXiv:1812.04754*, 2018.

[4] Ryo Karakida, Shotaro Akaho, and Shun-ichi Amari. Universal statistics of fisher information in deep neural networks: Mean field approach. In *The 22nd International Conference on Artificial Intelligence and Statistics*, pages 1032–1041. PMLR, 2019.

[5] Mohsen Soori, Behrooz Arezoo, and Roza Dastres. Artificial intelligence, machine learning and deep learning in advanced robotics, a review. *Cognitive Robotics*, 3:54–70, 2023.

[6] Asharul Islam Khan and Salim Al-Habsi. Machine learning in computer vision. *Procedia Computer Science*, 167:1444–1451, 2020.

[7] Amirsina Torfi, Rouzbeh A Shirvani, Yaser Keneshloo, Nader Tavaf, and Edward A Fox. Natural language processing advancements by deep learning: A survey. *arXiv preprint arXiv:2003.01200*, 2020.

[8] Song Han, Jeff Pool, John Tran, and William Dally. Learning both weights and connections for efficient neural network. *Advances in neural information processing systems*, 28, 2015.

[9] Hongrong Cheng, Miao Zhang, and Javen Qinfeng Shi. A survey on deep neural network pruning: Taxonomy, comparison, analysis, and recommendations. *IEEE Transactions on Pattern Analysis and Machine Intelligence*, 2024.

[10] Carole-Jean Wu, Ramya Raghavendra, Udit Gupta, Bilge Acun, Newsha Ardalani, Kiwan Maeng, Gloria Chang, Fiona Aga, Jinshi Huang, Charles Bai, et al. Sustainable ai: Environmental implications, challenges and opportunities. *Proceedings of Machine Learning and Systems*, 4: 795–813, 2022.

[11] Andrew A Chien, Liuzixuan Lin, Hai Nguyen, Varsha Rao, Tristan Sharma, and Rajini Wijayawardana. Reducing the carbon impact of generative ai inference (today and in 2035). In *Proceedings of the 2nd workshop on sustainable computer systems*, pages 1–7, 2023.

[12] Tim Dettmers, Artidoro Pagnoni, Ari Holtzman, and Luke Zettlemoyer. Qlora: efficient finetuning of quantized llms (2023). *arXiv preprint arXiv:2305.14314*, 52:3982–3992, 2023.

[13] Emily L Denton, Wojciech Zaremba, Joan Bruna, Yann LeCun, and Rob Fergus. Exploiting linear structure within convolutional networks for efficient evaluation. *Advances in neural information processing systems*, 27, 2014.

[14] Xiaohan Xu, Ming Li, Chongyang Tao, Tao Shen, Reynold Cheng, Jinyang Li, Can Xu, Dacheng Tao, and Tianyi Zhou. A survey on knowledge distillation of large language models. *arXiv preprint arXiv:2402.13116*, 2024.

[15] Miao Zhang, Steven W Su, Shirui Pan, Xiaojun Chang, Ehsan M Abbasnejad, and Reza Haffari. idarts: Differentiable architecture search with stochastic implicit gradients. In *International Conference on Machine Learning*, pages 12557–12566. PMLR, 2021.

[16] Tanishq Kumar, Kevin Luo, and Mark Sellke. No free prune: Information-theoretic barriers to pruning at initialization. *arXiv preprint arXiv:2402.01089*, 2024.

[17] Sidak Pal Singh and Dan Alistarh. Woodfisher: Efficient second-order approximation for neural network compression. *Advances in Neural Information Processing Systems*, 33:18098–18109, 2020.

[18] Jonathan Frankle and Michael Carbin. The lottery ticket hypothesis: Finding sparse, trainable neural networks. *arXiv preprint arXiv:1803.03635*, 2018.

[19] Kartik Sreenivasan, Jy-yong Sohn, Liu Yang, Matthew Grinde, Alliot Nagle, Hongyi Wang, Eric Xing, Kangwook Lee, and Dimitris Papailiopoulos. Rare gems: Finding lottery tickets at initialization. *Advances in neural information processing systems*, 35:14529–14540, 2022.

[20] Haoran You, Baopu Li, Zhanyi Sun, Xu Ouyang, and Yingyan Lin. Supertickets: Drawing task-agnostic lottery tickets from supernets via jointly architecture searching and parameter pruning. In *European Conference on Computer Vision*, pages 674–690. Springer, 2022.

[21] Namhoon Lee, Thalaiyasingam Ajanthan, and Philip HS Torr. Snip: Single-shot network pruning based on connection sensitivity. *arXiv preprint arXiv:1810.02340*, 2018.

[22] Chaoqi Wang, Guodong Zhang, and Roger Grosse. Picking winning tickets before training by preserving gradient flow. *arXiv preprint arXiv:2002.07376*, 2020.

[23] Hidenori Tanaka, Daniel Kunin, Daniel L Yamins, and Surya Ganguli. Pruning neural networks without any data by iteratively conserving synaptic flow. *Advances in neural information processing systems*, 33:6377–6389, 2020.

[24] Zhenyu Liao and Michael W Mahoney. Hessian eigenspectra of more realistic nonlinear models. *Advances in Neural Information Processing Systems*, 34:20104–20117, 2021.

[25] Yann LeCun. The mnist database of handwritten digits. *http://yann. lecun. com/exdb/mnist/*, 1998.

[26] Zhewei Yao, Amir Gholami, Sheng Shen, Mustafa Mustafa, Kurt Keutzer, and Michael Mahoney. Adahessian: An adaptive second order optimizer for machine learning. In *proceedings of the AAAI conference on artificial intelligence*, volume 35, pages 10665–10673, 2021.

[27] Jonathan Frankle, Gintare Karolina Dziugaite, Daniel M Roy, and Michael Carbin. Pruning neural networks at initialization: Why are we missing the mark? *arXiv preprint arXiv:2009.08576*, 2020.

[28] Barak A Pearlmutter. Fast exact multiplication by the hessian. *Neural computation*, 6(1):147–160, 1994.

[29] James Martens and Ilya Sutskever. Learning recurrent neural networks with hessian-free optimization. In *Proceedings of the 28th international conference on machine learning (ICML-11)*, pages 1033–1040, 2011.

[30] Nicol N Schraudolph. Fast curvature matrix-vector products for second-order gradient descent. *Neural computation*, 14(7):1723–1738, 2002.

[31] James Martens and Roger Grosse. Optimizing neural networks with kronecker-factored approximate curvature. In *International conference on machine learning*, pages 2408–2417. PMLR, 2015.

[32] Mohamed Elsayed, Homayoon Farrahi, Felix Dangel, and A Rupam Mahmood. Revisiting scalable hessian diagonal approximations for applications in reinforcement learning. *arXiv preprint arXiv:2406.03276*, 2024.

[33] James Martens, Ilya Sutskever, and Kevin Swersky. Estimating the hessian by backpropagating curvature. *arXiv preprint arXiv:1206.6464*, 2012.

[34] Cornelia Vacar, Jean-Françis Giovannelli, and Yannick Berthoumieu. Langevin and hessian with fisher approximation stochastic sampling for parameter estimation of structured covariance. In *2011 IEEE International Conference on Acoustics, Speech and Signal Processing (ICASSP)*, pages 3964–3967. IEEE, 2011.

[35] Mark J Schervish. *Theory of statistics*. Springer series in statistics. Springer, New York, NY, 1995 edition, December 2012.

[36] Alexander Soen and Ke Sun. Tradeoffs of diagonal fisher information matrix estimators. *arXiv preprint arXiv:2402.05379*, 2024.

[37] Stephen Hanson and Lorien Pratt. Comparing biases for minimal network construction with back-propagation. *Advances in neural information processing systems*, 1, 1988.

[38] Lucas Theis, Iryna Korshunova, Alykhan Tejani, and Ferenc Huszár. Faster gaze prediction with dense networks and fisher pruning. *arXiv preprint arXiv:1801.05787*, 2018.

[39] Liyang Liu, Shilong Zhang, Zhanghui Kuang, Aojun Zhou, Jing-Hao Xue, Xinjiang Wang, Yimin Chen, Wenming Yang, Qingmin Liao, and Wayne Zhang. Group fisher pruning for practical network compression. In *International Conference on Machine Learning*, pages 7021–7032. PMLR, 2021.

[40] Arthur Jacot, Franck Gabriel, and Clément Hongler. Neural tangent kernel: Convergence and generalization in neural networks. *Advances in neural information processing systems*, 31, 2018.

[41] Huan Wang, Can Qin, Yue Bai, Yulun Zhang, and Yun Fu. Recent advances on neural network pruning at initialization, 2022. URL `https://arxiv.org/abs/2103.06460`.

[42] Alex Krizhevsky, Geoffrey Hinton, et al. Learning multiple layers of features from tiny images, 2009.

[43] Jia Deng, Wei Dong, Richard Socher, Li-Jia Li, Kai Li, and Li Fei-Fei. Imagenet: A large-scale hierarchical image database. In *2009 IEEE conference on computer vision and pattern recognition*, pages 248–255. Ieee, 2009.

[44] Kaiming He, Xiangyu Zhang, Shaoqing Ren, and Jian Sun. Deep residual learning for image recognition. In *Proceedings of the IEEE conference on computer vision and pattern recognition*, pages 770–778, 2016.

[45] Karen Simonyan. Very deep convolutional networks for large-scale image recognition. *arXiv preprint arXiv:1409.1556*, 2014.

[46] Alexey Dosovitskiy, Lucas Beyer, Alexander Kolesnikov, Dirk Weissenborn, Xiaohua Zhai, Thomas Unterthiner, Mostafa Dehghani, Matthias Minderer, Georg Heigold, Sylvain Gelly, Jakob Uszkoreit, and Neil Houlsby. An image is worth 16x16 words: Transformers for image recognition at scale, 2021. URL `https://arxiv.org/abs/2010.11929`.

[47] Edouard Yvinec, Arnaud Dapogny, Matthieu Cord, and Kevin Bailly. Singe: Sparsity via integrated gradients estimation of neuron relevance. *Advances in Neural Information Processing Systems*, 35:35392–35403, 2022.

[48] Mingyuan Sun, Zheng Fang, Jiaxu Wang, Junjie Jiang, Delei Kong, Chenming Hu, Yuetong Fang, and Renjing Xu. Optimal brain apoptosis, 2025. URL `https://arxiv.org/abs/2502.17941`.

[49] Jingtong Su, Yihang Chen, Tianle Cai, Tianhao Wu, Ruiqi Gao, Liwei Wang, and Jason D Lee. Sanity-checking pruning methods: Random tickets can win the jackpot. *Advances in neural information processing systems*, 33:20390–20401, 2020.

Appendix

A. Hessian Spectrum

This section complements the curvature discussion in the main text by showing how parameter updates align with the Hessian's eigendirections at initialization in a small-scale setting. We consider binary classification in the MNIST [25] dataset, restricted to digits $(4, 7)$ (mapped to labels 0,1). The data is normalized using the standard MNIST statistics, and we use a batch size of 256. We use a two-layer fully connected network with 12,577 parameters initialized with Xavier-uniform weights and zero biases. We train for 10 epochs with SGD (learning rate 10^{-4}, momentum 0.9, weight decay 10^{-4}) and Cross-Entropy loss. For clarity, we will stick to the notation in the main body of the manuscript.

Hessian and Eigendecomposition at Initialization. At initialization w_0, we compute the full empirical Hessian column-wise using Hessian–vector products throughout the training set: for each basis vector $e_i \in \mathbb{R}^P$ we evaluate $H_0 e_i$ by differentiating a scalar product $g(w_0)^\top e_i$, where $g(w_0)$ is the mean loss gradient. The columns are accumulated and symmetrized as $(H_0 + H_0^\top)/2$. We then perform a dense symmetric eigendecomposition using Torch.

Parameter Projection in the Hessian Eigenbasis. We compute $\Delta w_t = w_t - w_0$ after the first optimization step and after the termination of each subsequent epoch. For each checkpoint, we flatten to $\mathbb{R}^P$, and project it onto the eigenbasis of H_0 to obtain $z_t = U_0^\top \Delta w_t$. We focus on the absolute coefficients $|z_{t,i}|$, which measure how far training has moved along the eigenvector i.

Figures A1 (a), (b), and (c) show the projection after the first optimization step, after epoch 1, and in epoch 5. In all three cases, most of the displacement mass is concentrated in the leading directions, while the remaining coordinates remain close to zero. The overall shape of this profile becomes visible after the first update and remains qualitatively stable throughout training, indicating that gradient-based optimization quickly becomes confined to a low-dimensional subspace spanned by the top eigendirections of the Hessian at (or very near) initialization.

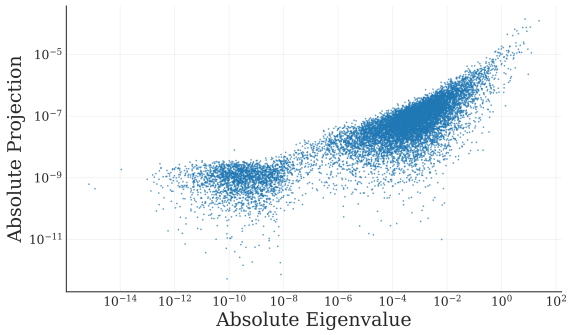

(a) Projection of Δw after the first optimization step.

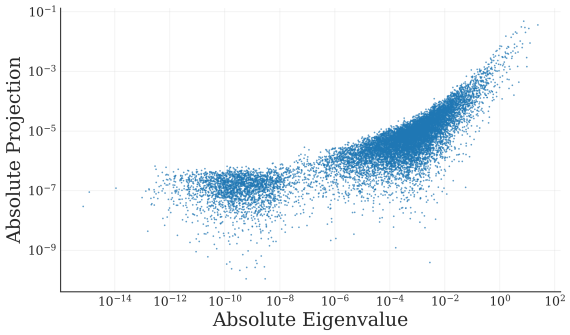

(b) Projection of Δw after the first training epoch.

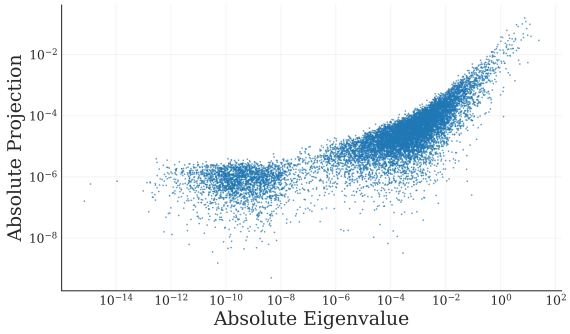

(c) Projection of Δw after the fifth training epoch.

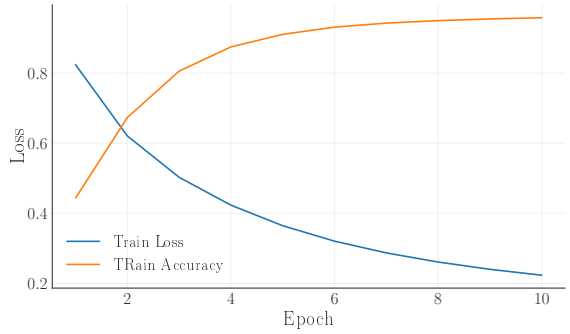

(d) Loss and Accuracy across training epochs for a single random seed.

Figure A1: Hessian spectrum and parameter displacement in the eigenbasis at different points in training. Loss and Accuracy progress throughout training.

B. Training and Testing Details

Following the setting in [49], we test after each training epoch and report the best top-1 test accuracy. Moreover, we ran each experiment on three seeds and reported the average test accuracy with the corresponding standard deviations. Table A1 shows the training parameters.

Table A1: Training configurations for various networks and datasets.

Network	Dataset	Epochs	Batch	Opt.	Mom.	LR	Weight Decay	LR Drops	Drop Factor
ResNet-18	CIFAR-10/100	160	512	SGD	0.9	0.03	5e-4	80, 120	0.2
ResNet-50	CIFAR-10	160	512	SGD	0.9	0.03	5e-4	80, 120	0.2
VGG-19	CIFAR-10/100	160	512	SGD	0.9	0.6	1e-4	80, 120	0.1
ResNet-18	TinyImageNet	100	512	SGD	0.9	0.03	1e-4	30, 60, 80	0.1
ResNet-50	ImageNet	90	256	SGD	0.9	0.1	1e-4	30, 60, 80	0.1

We conducted all CIFAR-10, CIFAR-100, and TinyImageNet experiments on a single NVIDIA RTX 5000 GPU. The ImageNet experiments were conducted in a distributed setting, utilizing 4 NVIDIA A100-SXM4 GPUs. Each GPU was assigned a batch size of 256 and a learning rate of 0.1. This corresponds to a global batch size of 1024 and a global learning rate of 0.4.

C. Computational Complexity

For clarity, we will stick to the notation in the main body of the manuscript: d denotes the number of parameters in the network, B is the number of batches, and N is the number of data samples. Following [27], we use a subset with 10 samples per class and a batch size of 1 to calculate the importance scores, so $B = N$. Given the small subset, the wall-clock time added to the training pipeline is negligible. Some precision about the columns:

- **Practical Time Complexity** corresponds to real computation, determined by the batch size used to create the mask and limited by available RAM/VRAM constraints.
- **Theoretical Time Complexity** indicates the worst-case scenario.
- **Space Complexity** indicates the storage requirements for estimating the metrics, considering that some require keeping intermediate results that will iteratively accumulate until the best metric estimation is obtained.

Table A2: Comparison of pruning methods in terms of computational complexity and runtime characteristics.

Method	Practical Time Complexity	Theoretical Time Complexity	Space Complexity	Depends on Data?	Uses Gradients?	Hessian Use
Random	$\mathcal{O}(1)$	$\mathcal{O}(1)$	$\mathcal{O}(1)$	No	No	None
Magnitude	$\mathcal{O}(d)$	$\mathcal{O}(d)$	$\mathcal{O}(d)$	No	No	None
GN	$\mathcal{O}(Bd)$	$\mathcal{O}(Nd)$	$\mathcal{O}(d)$	Yes	Yes	None
SNIP	$\mathcal{O}(Bd)$	$\mathcal{O}(Nd)$	$\mathcal{O}(d)$	Yes	Yes	None
Synflow	$\mathcal{O}(d)$	$\mathcal{O}(d)$	$\mathcal{O}(d)$	No	Yes	None
GraSP	$\mathcal{O}(Bd^2)$	$\mathcal{O}(Nd^2)$	$\mathcal{O}(d)$	Yes	Yes	Hessian-vector
FD	$\mathcal{O}(Bd)$	$\mathcal{O}(Nd)$	$\mathcal{O}(d)$	Yes	Yes	Diag. approx.$^{F^*}$
FP	$\mathcal{O}(Bd)$	$\mathcal{O}(Nd)$	$\mathcal{O}(d)$	Yes	Yes	Diag. approx.$^{F^*}$
FTS	$\mathcal{O}(Bd)$	$\mathcal{O}(Nd)$	$\mathcal{O}(d)$	Yes	Yes	Diag. approx.$^{F^*}$
HD	$\mathcal{O}(Bd)$	$\mathcal{O}(Nd)$	$\mathcal{O}(d)$	Yes	Yes	Diag. approx.$^{H^*}$
HP	$\mathcal{O}(Bd)$	$\mathcal{O}(Nd)$	$\mathcal{O}(d)$	Yes	Yes	Diag. approx.$^{H^*}$
HTS	$\mathcal{O}(Bd)$	$\mathcal{O}(Nd)$	$\mathcal{O}(d)$	Yes	Yes	Diag. approx.$^{H^*}$
OBD	$\mathcal{O}(Bd)$	$\mathcal{O}(Nd)$	$\mathcal{O}(d)$	Yes^a	Yes^b	Diag.^{a}
OBS	$\mathcal{O}(Bd^2)$	$\mathcal{O}(Nd^2)$	$\mathcal{O}(d^2)$	Yes^a	Yes^c	Full inverse^d
Full Hessian	$\mathcal{O}(Bd^2)$	$\mathcal{O}(Nd^2)$	$\mathcal{O}(d^2)$	Yes	Yes	Full

$^{F^*}$ FIM Approximation, $^{H^*}$ Hutchinson Approximation, ^{a} Post-Training, ^{b} For diagonal, ^{c} Outer products, ^{d} Kailath.

Notes:

1. Synflow does not depend on data, but calculates gradients based on a dummy input. Runtime linearly increases with the number of pruning steps to reach the target sparsity (fixed at 100 as in the original implementation).
2. F* methods use the empirical Fisher diagonal (computed from squared gradients on data batches), not the true Hessian. Practical runtime scales with the number of batches used for estimation.
3. H* methods use Hutchinson's stochastic diagonal approximation of the Hessian. The runtime scales linearly with the number of probe vectors (fixed at 10 here).
4. Depends on Data? indicates whether the method requires explicit forward/backward passes on input data to estimate its metric, not just parameter values.
5. Space Complexity: Entries such as $\mathcal{O}(d^2)$ (OBS, Full Hessian) are correct theoretically but infeasible in practice for modern networks, since storing the full Hessian or its inverse is memory-prohibitive.

D. Sensitivity Analysis on Number of Samples

As mentioned in Section C of the Appendix, we used a small subset of the data (10 samples per class) to compute the pruning scores following the protocol defined in [27], which in turn follows the work in [22], which argues it is a sufficiently large subset. To verify this assumption, we conducted experiments on the base reference case (CIFAR-10 on ResNet-18). First, we defined a single sparsity (95%). Then we evaluated data-dependent methods with an increasing number of samples per class, up to utilizing the whole training set (5k samples per class). We maintain a batch size of 1 for the score computation and use the same initialization seeds to ensure consistency with the experiments in the main body. We also incorporate the proposed warmup step, as it has been shown to improve method performance.

Table A3: Effect of the number of samples per class used to compute the pruning mask (CIFAR-10, ResNet-18, sparsity 0.95, batch size 1).

Samples per class	GN	SNIP	GraSP	**FD**	**FP**	**FTS**	**HD**	**HP**	**HTS**
1	92.56 ± 0.16	92.38 ± 0.04	91.18 ± 0.42	92.04 ± 0.13	92.07 ± 0.16	92.37 ± 0.17	92.47 ± 0.08	92.36 ± 0.11	92.36 ± 0.07
10	92.15 ± 0.33	92.19 ± 0.13	90.86 ± 0.30	79.83 ± 19.10	91.36 ± 0.34	92.27 ± 0.06	92.30 ± 0.23	92.32 ± 0.21	92.18 ± 0.37
100	91.28 ± 0.52	92.06 ± 0.15	90.48 ± 0.12	64.46 ± 2.90	91.43 ± 0.14	91.91 ± 0.30	92.36 ± 0.28	92.27 ± 0.24	92.28 ± 0.27
1000	90.03 ± 0.27	91.87 ± 0.18	90.80 ± 0.27	34.51 ± 42.46	91.16 ± 0.06	91.71 ± 0.17	92.42 ± 0.15	92.28 ± 0.24	92.15 ± 0.20
5000	89.87 ± 0.38	91.69 ± 0.23	90.76 ± 0.17	89.98 ± 0.28	91.75 ± 0.14	91.65 ± 0.20	92.45 ± 0.27	92.28 ± 0.10	92.13 ± 0.08

The results in Table A3 show that all criteria based on non-Hutchinson follow the same trend: as the number of samples for computation increases, there is a slight decrease in performance. FD is observed to suffer the most as the number of samples increases. However, Hutchinson-based criteria are more robust, further solidifying the value of second-order information. Given the defined trend, we question whether the batch size of 1 played a role in the lower performance when using the entire training set. In the same setup, we evaluated increasing the batch size for score computation (1, 10, 100, 1000). The selected batch sizes were defined to avoid mini-batches with fewer samples that misalign the average computation.

Table A4: Effect of batch size used to compute the pruning mask (CIFAR-10, ResNet-18, sparsity 0.95, 5K samples/class).

Batch size	GN	SNIP	GraSP	**FD**	**FP**	**FTS**	**HD**	**HP**	**HTS**
1	90.04 ± 0.30	91.63 ± 0.09	90.40 ± 0.35	34.25 ± 42.00	91.48 ± 0.08	91.86 ± 0.37	92.10 ± 0.12	92.34 ± 0.19	92.24 ± 0.15
10	89.97 ± 0.22	91.56 ± 0.24	90.69 ± 0.07	86.40 ± 3.60	91.52 ± 0.38	91.74 ± 0.24	92.44 ± 0.14	92.33 ± 0.12	92.01 ± 0.18
100	90.06 ± 0.12	91.80 ± 0.24	90.80 ± 0.26	90.82 ± 0.15	91.80 ± 0.11	91.91 ± 0.23	92.25 ± 0.15	92.25 ± 0.10	92.01 ± 0.17
1000	89.93 ± 0.41	91.60 ± 0.24	90.87 ± 0.19	90.57 ± 0.24	91.72 ± 0.13	91.73 ± 0.07	92.26 ± 0.15	92.39 ± 0.12	92.19 ± 0.16

The results in Table A4 show that batch size does not affect the previously observed trend, as all methods (except FD) produce close results regardless of the batch size. Still, we observe that increasing the batch size alleviates the performance drop of FD. Considering the heuristics involved, it is challenging to draw a definitive conclusion. However, we can offer a general recommendation to increase the batch size of score computation in the PaI setting if the practitioner chooses to utilize a larger subset, as this can prevent the performance drop observed in FD and accelerate computation time.

E. Sensitivity Analysis on Hutchinson Probes

Regarding the number of probes (random Rademacher vectors), we used a fixed number of 10 probes to compute the Hutchinson Diagonal (HD) approximation across all experiments. We defined this constant based on the linear increase in computation as the number of probes increased. We performed experiments in the same setting as the base case (10 samples per class), with the only change being the number of random probes used to compute the score.

Table A5: Effect of the number of random probes on Hutchinson diagonal mask computation (CIFAR-10, ResNet-18, sparsity 0.95).

No. Probes	Avg. Acc. (w/o warmup)	Avg. Acc. (w/ warmup)	Computation Time (s)
1	91.26 ± 0.15	92.37 ± 0.22	1.75
10	91.01 ± 0.33	92.36 ± 0.09	9.26
50	91.13 ± 0.02	92.44 ± 0.19	44.07
100	91.13 ± 0.15	92.18 ± 0.12	87.65

The results in Table A5 show that the approximation is very robust to the number of probes used; even a single probe is sufficient to find a performant subnetwork. The warmup step improved performance, but increasing the number of probes did not further improve performance, aligning with the AdaHessian implementation [26], which uses only one probe to compute the approximation used in the optimization step.

F. Study on Batch-Norm Statistics

All models in our experiments use batch normalization (BN) layers; however, only VGG-19 exhibits layer collapse. We presumed that better statistics yield better gradient estimations, which is paramount when using data-based criteria in pruning. To validate this insight, we ran an experiment comparing the resulting pruning masks before and after updating the BN statistics.

Table A6: Importance of batch normalization layers' statistics (BNS) in preventing layer collapse. We studied the case of VGG-19 pruning at 95% sparsity, which is the level that started showing layer collapse. *C* indicates the percentage of layers that collapsed after pruning (100% of the layer is pruned), and *B* indicates the percentage leading to a bottleneck (80% of the layer is pruned).

	GN		SNIP		GraSP		**FD**		**FP**		**FTS**		**HD**		**HP**		**HTS**	
BNS Status	C (%)	B (%)	C (%)	B (%)	C (%)	B (%)	C (%)	B (%)	C (%)	B (%)	C (%)	B (%)	C (%)	B (%)	C (%)	B (%)	C (%)	B (%)
Without Warmup	16.67	24.20	18.18	22.73	16.67	24.24	16.67	24.24	12.12	24.24	16.67	24.24	13.64	24.24	1.52	22.73	13.64	24.24
With Warmup	0	22.73	0	12.12	0	12.12	0	19.70	0	22.73	0	19.70	0	15.15	0	15.15	0	16.67

Table A6 compares the percentage of collapsed layers in VGG19 resulting from the pruning mask before and after updating only the BN statistics, with the initial parameters frozen, using a single pass through the data. Note that $\%C$ indicates the percentage of layers that collapsed after pruning $(100\%$ of the layer is pruned$)$, and $\%B$ indicates the percentage leading to a bottleneck $(80\%$ of the layer is pruned$)$. This insight allowed us to propose the warmup process to mitigate layer collapse.

G. Results CIFAR10

G.1. ResNet18

Table A7: Performance of different pruning methods for CIFAR-10 on ResNet-18 without warmup. Bold and underlined values highlight the top performer. Bold values show methods whose confidence intervals overlap with the best performer. Baseline accuracy (no pruning): 93.89 $\pm$ 0.33.

Sparsity (%)	Random	Magnitude	GN	SNIP	GraSP	SynFlow	FD	FP	FTS	HD	HP	HTS
10	**93.77 ± 0.15**	**93.81 ± 0.08**	**93.72 ± 0.15**	**93.68 ± 0.13**	92.84 ± 0.12	**93.89 ± 0.18**	**93.83 ± 0.24**	**93.77 ± 0.11**	**93.87 ± 0.01**	**93.86 ± 0.18**	**93.85 ± 0.05**	**93.73 ± 0.15**
20	**93.81 ± 0.17**	**93.70 ± 0.09**	**93.86 ± 0.25**	**93.74 ± 0.18**	92.69 ± 0.26	93.63 ± 0.06	**93.67 ± 0.19**	**93.82 ± 0.18**	**93.78 ± 0.08**	**93.69 ± 0.20**	**93.72 ± 0.18**	**93.87 ± 0.14**
30	**93.81 ± 0.05**	**93.75 ± 0.15**	**93.77 ± 0.08**	**93.77 ± 0.17**	92.69 ± 0.08	93.45 ± 0.11	93.58 ± 0.07	**93.66 ± 0.22**	**93.80 ± 0.06**	**93.77 ± 0.10**	**93.58 ± 0.29**	**93.79 ± 0.18**
40	**93.58 ± 0.07**	**93.63 ± 0.09**	**93.70 ± 0.13**	**93.58 ± 0.06**	92.45 ± 0.05	**93.71 ± 0.12**	**93.55 ± 0.14**	**93.93 ± 0.29**	**93.74 ± 0.07**	**93.64 ± 0.12**	**93.55 ± 0.14**	**93.73 ± 0.12**
50	93.54 ± 0.22	93.58 ± 0.14	**93.64 ± 0.16**	93.55 ± 0.16	92.37 ± 0.24	93.62 ± 0.05	**93.58 ± 0.21**	**93.89 ± 0.11**	93.65 ± 0.12	93.52 ± 0.04	93.52 ± 0.16	93.61 ± 0.16
60	93.42 ± 0.09	**93.67 ± 0.09**	**93.48 ± 0.09**	**93.56 ± 0.22**	92.34 ± 0.25	**93.79 ± 0.24**	**93.51 ± 0.09**	**93.48 ± 0.24**	**93.56 ± 0.19**	93.41 ± 0.14	93.45 ± 0.05	**93.70 ± 0.17**
70	93.18 ± 0.16	**93.59 ± 0.10**	**93.45 ± 0.07**	**93.60 ± 0.25**	92.02 ± 0.07	10.00 ± 0.00	**93.39 ± 0.11**	**93.38 ± 0.13**	**93.50 ± 0.10**	**93.28 ± 0.14**	**93.54 ± 0.03**	**93.36 ± 0.21**
80	92.64 ± 0.23	**93.35 ± 0.09**	**93.22 ± 0.06**	**93.29 ± 0.04**	92.06 ± 0.34	10.00 ± 0.00	92.86 ± 0.08	**93.26 ± 0.11**	**93.30 ± 0.07**	93.01 ± 0.17	**93.00 ± 0.36**	**93.14 ± 0.16**
90	91.38 ± 0.16	**92.86 ± 0.11**	92.35 ± 0.22	92.73 ± 0.08	91.88 ± 0.37	10.00 ± 0.00	91.85 ± 0.07	92.49 ± 0.23	**92.94 ± 0.08**	92.26 ± 0.12	92.70 ± 0.10	**92.84 ± 0.19**
95	89.59 ± 0.41	**92.05 ± 0.22**	91.43 ± 0.21	**91.70 ± 0.28**	91.27 ± 0.22	10.00 ± 0.00	90.40 ± 0.20	91.66 ± 0.12	**91.92 ± 0.15**	91.20 ± 0.06	**92.06 ± 0.22**	**91.97 ± 0.20**
98	86.29 ± 0.22	88.45 ± 0.14	89.03 ± 0.14	89.86 ± 0.25	90.01 ± 0.18	10.00 ± 0.00	88.11 ± 0.37	89.54 ± 0.02	89.82 ± 0.08	88.98 ± 0.23	**90.46 ± 0.14**	89.87 ± 0.37
99	82.92 ± 0.23	76.54 ± 0.24	86.70 ± 0.53	87.61 ± 0.39	**88.19 ± 0.41**	10.00 ± 0.00	84.98 ± 0.12	86.52 ± 0.24	87.55 ± 0.21	87.39 ± 0.34	**88.39 ± 0.06**	87.73 ± 0.19

Table A7 shows the complete sparsity spectrum for ResNet-18 with CIFAR-10. We highlight the model's resilience, as random pruning results in negligible performance drops up to 60% sparsity compared to the baseline. After this point, we observe a significant degradation for naive methods (random and magnitude). The proposed second-order-based criteria (in bold) demonstrate robustness, consistently ranking among the top performers across sparsity ratios.

Table A8: Performance of different pruning methods for CIFAR-10 on ResNet-18 with warmup. Bold and underlined values highlight the top performer. Bold values indicate methods whose confidence intervals overlap with those of the best performer.

Sparsity (%)	GN	SNIP	GraSP	SynFlow	FD	FP	FTS	HD	HP	HTS
80	**93.32 ± 0.12**	**93.30 ± 0.24**	91.73 ± 0.46	10.00 ± 0.00	**93.52 ± 0.17**	**93.36 ± 0.08**	**93.47 ± 0.30**	**93.28 ± 0.08**	**93.32 ± 0.10**	**93.52 ± 0.03**
90	**92.71 ± 0.27**	**93.12 ± 0.02**	91.59 ± 0.06	10.00 ± 0.00	92.89 ± 0.04	**93.09 ± 0.26**	**93.00 ± 0.19**	92.64 ± 0.19	**92.87 ± 0.26**	**93.15 ± 0.21**
95	**92.16 ± 0.08**	**92.32 ± 0.16**	90.89 ± 0.29	10.00 ± 0.00	**79.58 ± 18.25**	91.52 ± 0.16	**92.27 ± 0.10**	**92.20 ± 0.13**	**92.18 ± 0.08**	**92.23 ± 0.31**
98	90.28 ± 0.22	90.29 ± 0.25	89.78 ± 0.14	10.00 ± 0.00	10.00 ± 0.00	89.31 ± 0.14	90.27 ± 0.07	**91.24 ± 0.27**	90.55 ± 0.18	90.25 ± 0.22
99	60.07 ± 43.38	88.36 ± 0.44	87.98 ± 0.25	10.00 ± 0.00	10.00 ± 0.00	85.39 ± 0.34	88.02 ± 0.17	**89.47 ± 0.15**	88.79 ± 0.20	88.06 ± 0.20

Table A8 shows how the proposed warmup step improves the gradient estimation and improves the performance of first- and second-order criteria. Notably, HD shows a significant improvement in performance.

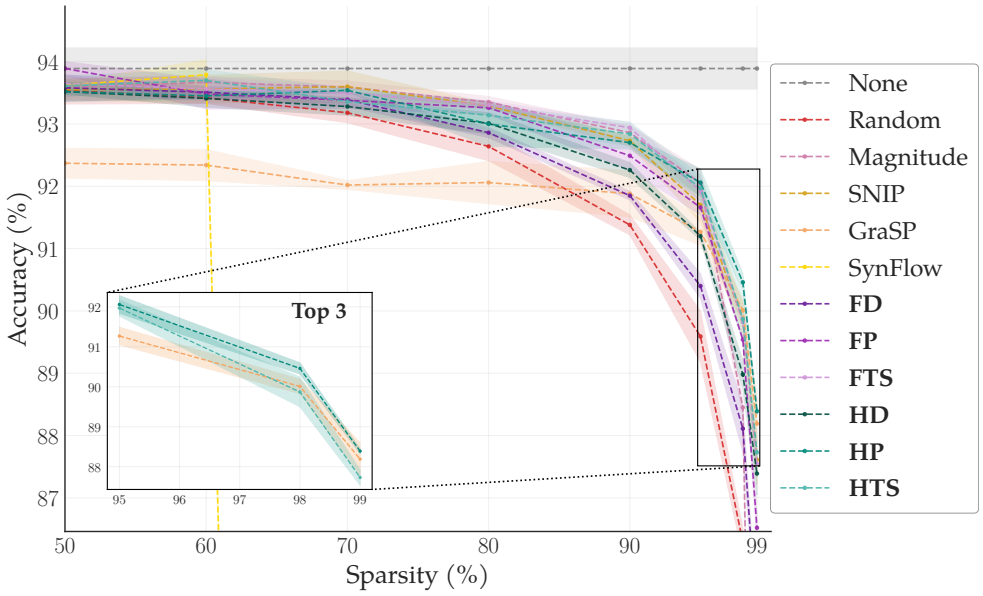

(a) Without warmup

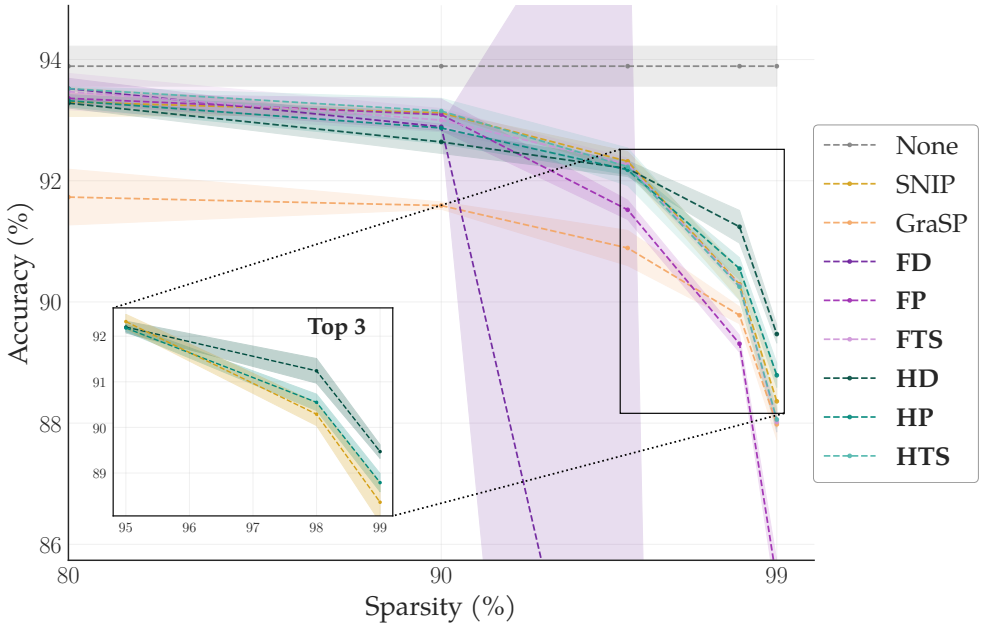

(b) With warmup

Figure A2: Test accuracy for ResNet-18 for the CIFAR-10 dataset with and without warmup. For extreme sparsities, we zoom in on the top 3 performers.

G.2. VGG19

Table A9: Performance of different pruning methods for CIFAR-10 on VGG-19 without warmup. Bold and underlined values highlight the top performer. Bold values show methods whose confidence intervals overlap with the best performer. Baseline accuracy (no pruning): 91.57 $\pm$ 0.19.

Sparsity (%)	Random	Magnitude	GN	SNIP	GraSP	SynFlow	FD	FP	FTS	HD	HP	HTS
10	91.46 ± 0.46	**90.90 ± 1.50**	**91.91 ± 0.35**	**91.95 ± 0.26**	**64.12 ± 46.87**	**92.36 ± 0.36**	**91.96 ± 0.16**	**91.87 ± 0.28**	**64.53 ± 47.23**	**91.31 ± 0.87**	**91.40 ± 0.61**	91.76 ± 0.16
20	**91.58 ± 0.30**	91.11 ± 0.54	**90.27 ± 3.09**	**91.91 ± 0.20**	**64.41 ± 47.12**	10.00 ± 0.00	**92.08 ± 0.18**	**92.09 ± 0.15**	**90.60 ± 3.09**	**89.58 ± 3.07**	91.14 ± 0.26	**92.17 ± 0.33**
30	91.42 ± 0.48	**91.89 ± 0.28**	37.36 ± 47.39	91.93 ± 0.07	10.00 ± 0.00	10.00 ± 0.00	**91.82 ± 0.50**	**92.09 ± 0.17**	**92.13 ± 0.03**	91.74 ± 0.20	91.85 ± 0.18	**90.19 ± 3.25**
40	91.68 ± 0.18	**91.60 ± 0.42**	**92.19 ± 0.29**	**92.07 ± 0.19**	**57.55 ± 42.32**	10.00 ± 0.00	**92.11 ± 0.20**	**92.09 ± 0.11**	**89.85 ± 4.13**	91.58 ± 0.14	**90.30 ± 2.37**	**92.16 ± 0.22**
50	90.94 ± 0.39	**90.61 ± 1.80**	**92.03 ± 0.45**	**90.73 ± 2.14**	**64.21 ± 46.95**	10.00 ± 0.00	**92.02 ± 0.37**	**92.15 ± 0.32**	**92.00 ± 0.34**	**91.82 ± 0.33**	91.67 ± 0.28	**92.25 ± 0.25**
60	90.95 ± 0.42	**91.53 ± 0.72**	**92.16 ± 0.26**	**64.87 ± 47.52**	37.14 ± 47.00	10.00 ± 0.00	**92.09 ± 0.13**	**92.20 ± 0.11**	**92.21 ± 0.21**	**64.56 ± 47.25**	37.31 ± 47.30	**92.09 ± 0.06**
70	90.72 ± 0.10	**90.32 ± 2.33**	**92.25 ± 0.39**	**92.04 ± 0.14**	91.27 ± 0.58	10.00 ± 0.00	91.49 ± 0.27	**91.55 ± 0.49**	**64.48 ± 47.18**	**64.51 ± 47.21**	**92.19 ± 0.27**	**91.76 ± 0.16**
80	**63.26 ± 46.09**	**91.58 ± 0.14**	90.23 ± 0.18	90.98 ± 0.19	**64.39 ± 47.10**	10.00 ± 0.00	10.00 ± 0.00	83.95 ± 0.31	**91.24 ± 0.66**	**91.65 ± 0.30**	**64.44 ± 47.15**	90.50 ± 0.10
90	88.12 ± 1.63	**91.54 ± 0.10**	10.00 ± 0.00	10.00 ± 0.00	**59.96 ± 43.27**	10.00 ± 0.00	10.00 ± 0.00	10.00 ± 0.00	64.24 ± 18.53	10.00 ± 0.00	88.84 ± 0.39	10.00 ± 0.00
95	**86.45 ± 0.92**	10.00 ± 0.00	10.00 ± 0.00	10.00 ± 0.00	10.00 ± 0.00	10.00 ± 0.00	10.00 ± 0.00	10.00 ± 0.00	10.00 ± 0.00	10.00 ± 0.00	10.00 ± 0.00	10.00 ± 0.00
98	**82.58 ± 2.12**	10.00 ± 0.00	10.00 ± 0.00	10.00 ± 0.00	10.00 ± 0.00	10.00 ± 0.00	10.00 ± 0.00	10.00 ± 0.00	10.00 ± 0.00	10.00 ± 0.00	10.00 ± 0.00	10.00 ± 0.00
99	**78.18 ± 2.27**	10.00 ± 0.00	10.00 ± 0.00	10.00 ± 0.00	10.00 ± 0.00	10.00 ± 0.00	10.00 ± 0.00	10.00 ± 0.00	10.00 ± 0.00	10.00 ± 0.00	10.00 ± 0.00	10.00 ± 0.00

Table A10: Performance of different pruning methods for CIFAR-10 on VGG-19 with warmup. Bold and underlined values highlight the top performer. Bold values show methods whose confidence intervals overlap with the best performer.

Sparsity (%)	GN	SNIP	GraSP	SynFlow	FD	FP	FTS	HD	HP	HTS
80	**90.75 ± 2.09**	**91.69 ± 0.83**	90.74 ± 0.64	10.00 ± 0.00	**92.37 ± 0.35**	**91.09 ± 1.53**	89.75 ± 2.14	91.47 ± 0.12	91.14 ± 0.36	**91.85 ± 0.23**
90	92.04 ± 0.47	91.95 ± 0.16	90.98 ± 0.45	10.00 ± 0.00	46.87 ± 41.19	**93.04 ± 0.14**	**64.46 ± 47.17**	91.18 ± 0.20	91.00 ± 0.38	91.62 ± 0.48
95	**92.25 ± 0.19**	**91.89 ± 0.70**	90.58 ± 0.19	10.00 ± 0.00	10.00 ± 0.00	10.00 ± 0.00	**92.04 ± 0.35**	91.24 ± 0.26	91.05 ± 0.35	91.52 ± 0.47
98	59.50 ± 43.46	37.15 ± 47.03	**90.63 ± 0.42**	10.00 ± 0.00	10.00 ± 0.00	10.00 ± 0.00	23.68 ± 23.69	**90.17 ± 0.58**	**90.38 ± 0.26**	32.14 ± 23.81
99	10.00 ± 0.00	10.00 ± 0.00	**89.10 ± 0.37**	10.00 ± 0.00	10.00 ± 0.00	10.00 ± 0.00	10.00 ± 0.00	**89.06 ± 0.36**	66.05 ± 7.84	10.00 ± 0.00

Table A9 shows the complete sparsity spectrum for VGG-19 with CIFAR-10. We observe that performance drastically degrades for data-dependent methods as sparsity increases, ultimately leading to layer collapse. As discussed in the Results section of the main body, we propose a warmup phase that updates the batch norm statistics to prevent collapse and stabilize pruning performance. Table A10 demonstrates the effectiveness of this approach to mitigate layer collapse.

G.3. ResNet50

Table A11: Performance of different pruning methods for CIFAR-10 on ResNet-50 without warmup. Bold and underlined values highlight the top performer. Bold values indicate methods whose confidence intervals overlap with those of the best performer. Baseline accuracy (no pruning): 93.17 ± 0.25.

Sparsity (%)	Random	Magnitude	GN	SNIP	GraSP	SynFlow	FD	FP	FTS	HD	HP	HTS
10	**93.52 ± 0.18**	**93.63 ± 0.22**	**93.45 ± 0.19**	**93.45 ± 0.34**	91.91 ± 0.13	**93.80 ± 0.47**	**93.50 ± 0.30**	**93.23 ± 0.26**	92.91 ± 0.15	**92.78 ± 1.05**	92.96 ± 0.26	**93.35 ± 0.70**
20	92.91 ± 0.38	93.23 ± 0.35	93.27 ± 0.16	93.34 ± 0.18	90.70 ± 1.12	**93.92 ± 0.13**	92.95 ± 0.07	92.96 ± 0.52	93.43 ± 0.04	92.91 ± 0.82	93.24 ± 0.33	**93.40 ± 0.55**
30	93.32 ± 0.14	93.11 ± 0.11	92.82 ± 0.56	93.21 ± 0.47	90.72 ± 2.88	**94.07 ± 0.06**	93.01 ± 0.35	93.19 ± 0.10	93.36 ± 0.31	92.90 ± 0.42	93.10 ± 0.32	93.24 ± 0.14
40	93.20 ± 0.03	93.18 ± 0.36	93.07 ± 0.34	92.96 ± 0.51	87.50 ± 4.27	**94.20 ± 0.06**	93.11 ± 0.76	92.91 ± 0.21	93.24 ± 0.47	93.15 ± 0.42	93.32 ± 0.15	93.42 ± 0.21
50	93.05 ± 0.51	93.25 ± 0.38	93.22 ± 0.33	92.98 ± 0.62	89.63 ± 2.63	**94.28 ± 0.01**	93.01 ± 0.48	93.18 ± 0.30	93.01 ± 0.31	92.98 ± 0.29	93.11 ± 0.37	93.14 ± 0.40
60	**93.07 ± 0.47**	**92.93 ± 0.84**	**93.18 ± 0.40**	**93.43 ± 0.61**	88.74 ± 2.41	10.00 ± 0.00	**93.01 ± 0.22**	**93.01 ± 0.46**	**93.07 ± 0.15**	**93.18 ± 0.57**	**93.16 ± 0.38**	**93.02 ± 0.40**
70	93.17 ± 0.16	**93.78 ± 0.15**	92.83 ± 0.33	92.96 ± 0.41	87.86 ± 2.54	10.00 ± 0.00	92.45 ± 0.54	91.82 ± 0.63	92.94 ± 0.13	93.30 ± 0.13	93.16 ± 0.11	92.96 ± 0.01
80	**92.71 ± 0.31**	90.88 ± 0.21	**93.00 ± 0.09**	92.29 ± 0.10	89.63 ± 2.43	10.00 ± 0.00	92.32 ± 0.49	92.67 ± 0.06	**92.79 ± 0.43**	92.69 ± 0.10	**93.13 ± 0.16**	92.29 ± 0.18
90	91.80 ± 0.10	80.13 ± 0.22	92.51 ± 0.10	92.18 ± 0.23	88.76 ± 1.14	10.00 ± 0.00	91.75 ± 0.06	92.19 ± 0.17	**92.73 ± 0.04**	92.18 ± 0.08	**92.54 ± 0.35**	92.32 ± 0.36
95	89.94 ± 0.23	10.00 ± 0.00	90.32 ± 0.29	**91.57 ± 0.31**	87.69 ± 1.71	10.00 ± 0.00	88.18 ± 0.60	91.05 ± 0.21	**91.80 ± 0.11**	90.80 ± 0.33	**91.43 ± 0.39**	**91.38 ± 0.35**
98	86.96 ± 0.38	10.00 ± 0.00	81.79 ± 1.48	**88.53 ± 0.30**	**88.38 ± 0.61**	10.00 ± 0.00	69.92 ± 4.22	85.49 ± 0.18	**88.31 ± 0.20**	87.65 ± 0.57	**88.90 ± 0.55**	**88.42 ± 0.21**
99	66.14 ± 27.98	10.00 ± 0.00	66.28 ± 3.00	82.41 ± 0.99	**85.96 ± 0.32**	10.00 ± 0.00	52.05 ± 2.02	74.83 ± 2.06	82.15 ± 0.88	79.84 ± 0.86	84.02 ± 0.78	83.70 ± 0.36

Table A11 shows the complete sparsity spectrum for ResNet-50 with CIFAR-10. Compared to the smaller ResNet-18, this deeper, wider architecture exhibits a faster decline in performance as sparsity increases. Notably, the SynFlow criterion performs well for low sparsities but suffers from layer collapse as sparsity increases. The proposed HP criteria (in bold) remain top performers for high sparsity levels, reinforcing the idea that there is no silver bullet for PaI, and that criteria are complementary. However, we emphasize that our proposed criteria effectively cover a broader part of the spectrum.

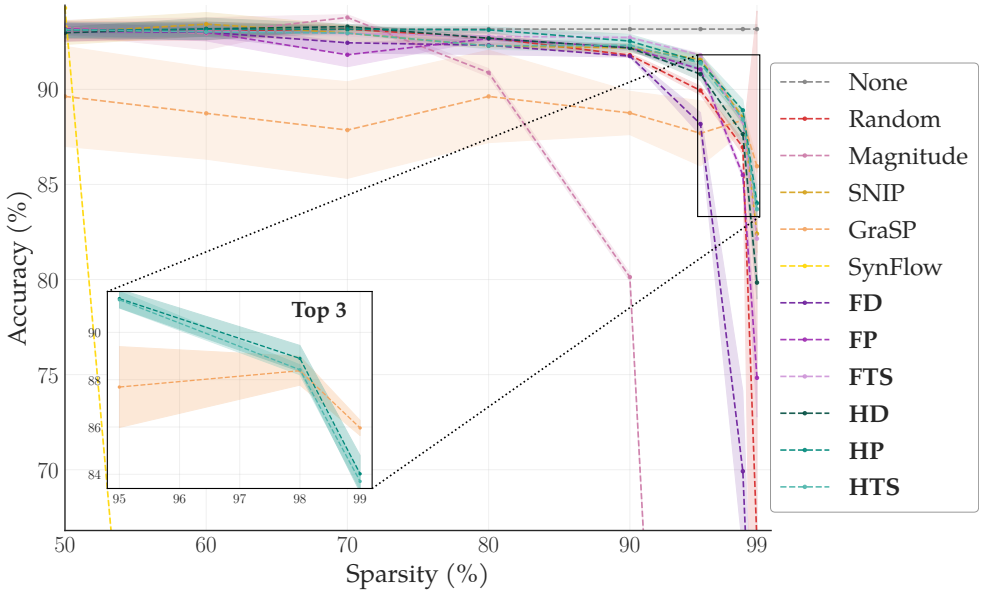

Figure A3: Test accuracy for ResNet-50 for the CIFAR-10 dataset only without warmup. For extreme sparsities, we zoom in on the top 3 performers.

H. Results CIFAR100

H.1. ResNet18

Table A12: Performance of different pruning methods for CIFAR-100 on ResNet-18 without warmup. Bold and underlined values highlight the top performer. Bold values show methods whose confidence intervals overlap with the best performer. Baseline accuracy (no pruning): 74.19 $\pm$ 0.14.

Sparsity (%)	Random	Magnitude	GN	SNIP	GraSP	SynFlow	FD	FP	FTS	HD	HP	HTS
10	**74.19 ± 0.28**	**74.51 ± 0.14**	74.25 ± 0.06	**74.50 ± 0.18**	71.35 ± 0.41	**74.49 ± 0.53**	**74.37 ± 0.30**	**74.55 ± 0.15**	**74.40 ± 0.13**	74.06 ± 0.32	74.09 ± 0.08	**74.35 ± 0.34**
20	**74.19 ± 0.44**	74.06 ± 0.03	**74.40 ± 0.34**	73.93 ± 0.18	71.34 ± 0.16	73.80 ± 0.16	74.06 ± 0.14	**74.31 ± 0.39**	**74.43 ± 0.10**	74.00 ± 0.08	73.92 ± 0.26	**74.39 ± 0.05**
30	**74.11 ± 0.09**	**74.18 ± 0.39**	**74.14 ± 0.03**	**73.89 ± 0.33**	70.82 ± 0.32	**73.83 ± 0.52**	**74.11 ± 0.15**	**74.21 ± 0.17**	**74.28 ± 0.21**	**73.96 ± 0.16**	**73.96 ± 0.25**	**74.16 ± 0.57**
40	73.69 ± 0.27	73.85 ± 0.12	73.90 ± 0.13	73.90 ± 0.14	70.09 ± 0.16	**73.78 ± 0.40**	73.87 ± 0.19	**74.37 ± 0.26**	**73.97 ± 0.36**	73.71 ± 0.20	73.75 ± 0.10	**74.18 ± 0.27**
50	**73.55 ± 0.18**	**73.82 ± 0.49**	**73.59 ± 0.25**	**73.86 ± 0.51**	70.33 ± 0.52	**73.55 ± 0.26**	73.25 ± 0.04	**73.59 ± 0.30**	**74.00 ± 0.32**	**73.62 ± 0.25**	**73.45 ± 0.30**	**73.99 ± 0.25**
60	**73.28 ± 0.27**	73.09 ± 0.26	**73.51 ± 0.29**	**73.16 ± 0.41**	69.80 ± 0.63	**73.38 ± 0.14**	72.70 ± 0.35	**73.54 ± 0.15**	**73.25 ± 0.17**	73.24 ± 0.11	**73.21 ± 0.22**	**73.29 ± 0.15**
70	72.49 ± 0.12	**73.30 ± 0.22**	72.61 ± 0.19	72.91 ± 0.14	69.70 ± 0.27	1.00 ± 0.00	71.84 ± 0.33	72.48 ± 0.05	72.82 ± 0.06	72.87 ± 0.05	72.78 ± 0.28	**72.83 ± 0.41**
80	71.07 ± 0.30	**72.49 ± 0.31**	71.34 ± 0.19	**72.16 ± 0.20**	69.30 ± 0.39	1.00 ± 0.00	70.85 ± 0.37	71.53 ± 0.09	71.53 ± 0.19	71.42 ± 0.13	71.80 ± 0.18	71.98 ± 0.08
90	68.46 ± 0.21	**70.17 ± 0.15**	68.81 ± 0.35	69.88 ± 0.05	67.72 ± 0.27	1.00 ± 0.00	68.64 ± 0.24	69.70 ± 0.15	**70.07 ± 0.31**	69.10 ± 0.36	**70.20 ± 0.20**	**69.97 ± 0.42**
95	64.17 ± 0.23	67.54 ± 0.24	67.46 ± 0.31	**67.70 ± 0.85**	66.32 ± 0.43	1.00 ± 0.00	66.48 ± 0.16	67.63 ± 0.20	67.65 ± 0.46	66.68 ± 0.39	**68.47 ± 0.31**	67.69 ± 0.33
98	59.72 ± 0.69	63.51 ± 0.20	63.12 ± 0.38	64.51 ± 0.47	63.83 ± 0.43	1.00 ± 0.00	62.06 ± 0.45	64.63 ± 0.10	64.70 ± 0.37	64.01 ± 0.11	**65.23 ± 0.14**	64.57 ± 0.12
99	53.23 ± 0.08	49.15 ± 0.32	57.23 ± 0.45	59.43 ± 0.24	59.60 ± 0.43	1.00 ± 0.00	54.24 ± 0.66	58.02 ± 0.28	59.73 ± 0.33	59.79 ± 0.33	**61.63 ± 0.59**	60.29 ± 0.14

We tested the CIFAR-100 dataset to extend our evaluation with a higher-complexity task. Table A12 shows that although some of our proposed metrics remain top performers at high to extreme sparsities. Additionally, HP criteria stand out significantly from the rest in the extreme sparsity setting, suggesting that second-order information could capture relevant features to push the boundaries of PaI forward.

Table A13: Performance of different pruning methods for CIFAR-100 on ResNet-18 with warmup. Bold and underlined values highlight the top performer. Bold values show methods whose confidence intervals overlap with the best performer.

Sparsity (%)	GN	SNIP	GraSP	SynFlow	FD	FP	FTS	HD	HP	HTS
80	71.85 ± 0.31	**72.43 ± 0.26**	69.60 ± 0.36	1.00 ± 0.00	70.56 ± 0.47	**72.52 ± 0.34**	**72.68 ± 0.12**	72.22 ± 0.14	**72.23 ± 0.38**	**72.69 ± 0.13**
90	69.78 ± 0.19	70.36 ± 0.34	68.30 ± 0.52	1.00 ± 0.00	65.46 ± 0.82	70.04 ± 0.26	**70.68 ± 0.25**	**70.77 ± 0.34**	**71.01 ± 0.54**	**71.19 ± 0.27**
95	66.85 ± 0.49	68.04 ± 0.27	66.71 ± 0.75	1.00 ± 0.00	2.07 ± 1.86	65.20 ± 0.32	67.75 ± 0.14	**69.45 ± 0.29**	68.61 ± 0.27	68.20 ± 0.16
98	58.96 ± 0.91	63.73 ± 0.66	63.06 ± 0.26	1.00 ± 0.00	1.00 ± 0.00	62.84 ± 0.66	63.78 ± 0.21	**66.38 ± 0.30**	65.65 ± 0.03	64.45 ± 0.15
99	14.97 ± 10.97	59.56 ± 0.25	57.34 ± 0.74	1.00 ± 0.00	1.00 ± 0.00	29.25 ± 16.18	59.17 ± 0.44	**62.08 ± 0.35**	61.23 ± 0.35	60.72 ± 0.29

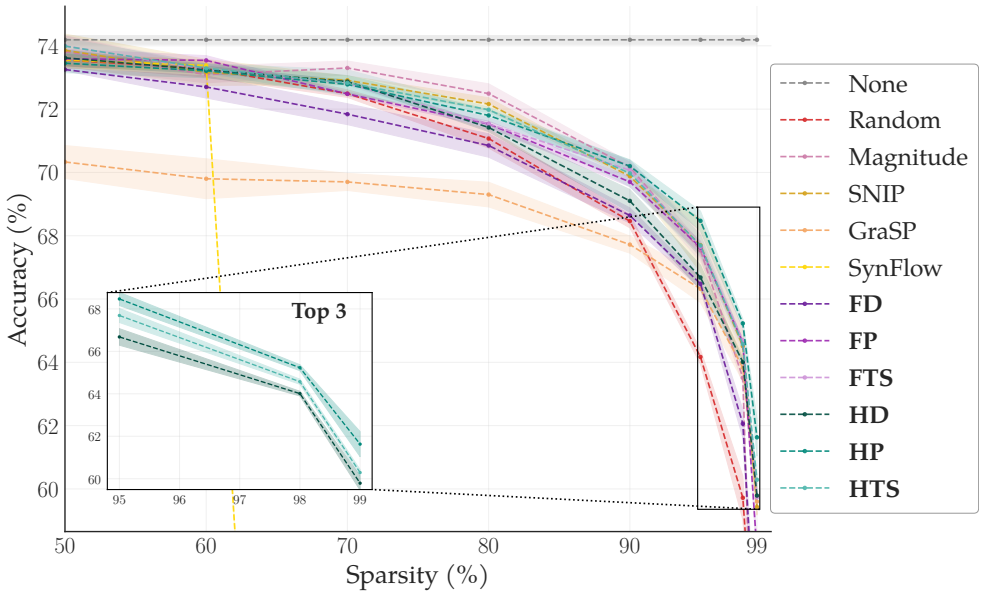

(a) Without warmup

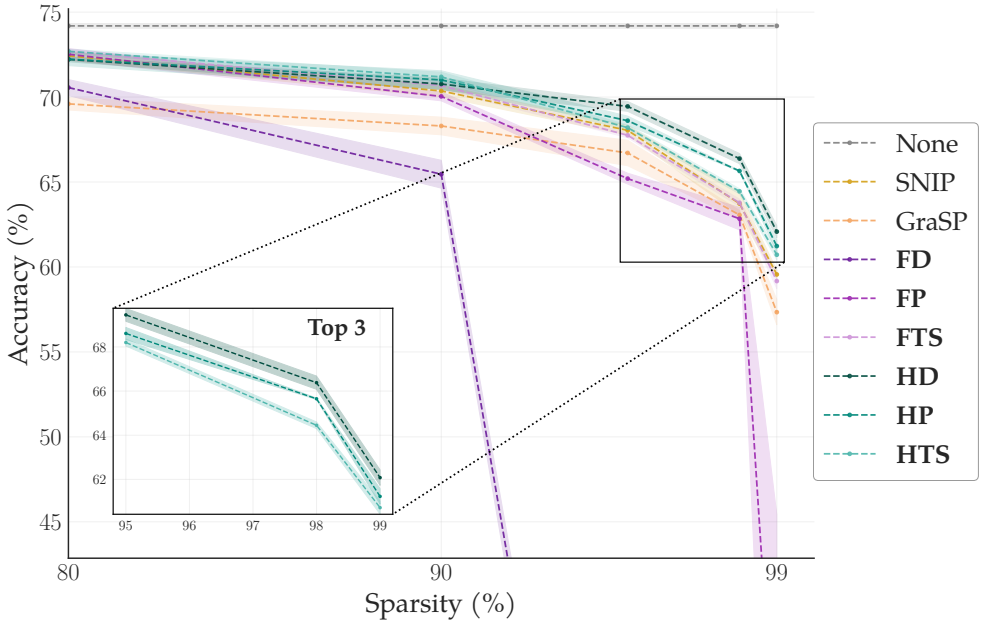

(b) With warmup

Figure A4: Test accuracy for ResNet-18 for the CIFAR-100 dataset with and without warmup. For extreme sparsities, we zoom in on the top 3 performers.

H.2. VGG19

Table A14: Performance of different pruning methods for CIFAR-100 on VGG-19 without warmup. Bold and underlined values highlight the top performer. Bold values show methods whose confidence intervals overlap with the best performer. Baseline accuracy (no pruning): 67.92 ± 0.86.

Sparsity (%)	Random	Magnitude	GN	SNIP	GraSP	SynFlow	FD	FP	FTS	HD	HP	HTS
10	66.94 ± 2.19	67.17 ± 0.05	**68.96 ± 0.72**	68.48 ± 0.64	66.19 ± 0.51	**69.69 ± 0.19**	68.08 ± 0.55	68.42 ± 0.94	68.16 ± 1.02	67.39 ± 1.04	67.92 ± 0.18	68.54 ± 0.83
20	**67.33 ± 1.32**	**67.51 ± 0.50**	**68.28 ± 0.66**	**45.11 ± 38.24**	**68.17 ± 0.64**	1.00 ± 0.00	**45.11 ± 38.20**	**68.36 ± 0.97**	**68.21 ± 0.34**	**67.39 ± 0.57**	**67.50 ± 0.67**	**67.82 ± 0.95**
30	**44.64 ± 37.81**	**68.23 ± 0.68**	**68.17 ± 0.72**	**45.37 ± 38.44**	**67.99 ± 0.60**	1.00 ± 0.00	**67.61 ± 0.32**	**68.11 ± 0.71**	**68.00 ± 1.03**	**68.38 ± 0.70**	**68.35 ± 0.36**	**67.94 ± 0.32**
40	67.24 ± 0.46	**68.13 ± 0.43**	**46.31 ± 39.25**	**68.77 ± 0.43**	**68.03 ± 0.92**	1.00 ± 0.00	**68.38 ± 0.71**	**45.61 ± 38.65**	**68.81 ± 0.99**	**68.25 ± 0.83**	**68.11 ± 0.75**	**46.18 ± 39.12**
50	**67.16 ± 1.15**	**67.41 ± 1.33**	**67.52 ± 2.24**	**68.72 ± 0.80**	**45.40 ± 38.45**	1.00 ± 0.00	**67.93 ± 2.00**	**67.62 ± 1.67**	**68.49 ± 0.76**	**68.67 ± 0.73**	**67.93 ± 0.44**	**66.12 ± 4.87**
60	67.57 ± 0.43	67.97 ± 0.64	**68.68 ± 0.72**	**67.53 ± 1.91**	67.90 ± 0.63	1.00 ± 0.00	**68.22 ± 0.82**	**68.61 ± 0.85**	**68.21 ± 1.67**	**68.67 ± 0.37**	**68.76 ± 0.12**	**68.30 ± 1.25**
70	67.30 ± 0.06	**68.58 ± 1.02**	67.19 ± 0.04	66.23 ± 1.13	**67.72 ± 1.34**	1.00 ± 0.00	66.12 ± 1.51	67.03 ± 0.16	66.68 ± 0.40	**68.79 ± 0.16**	68.19 ± 0.20	67.10 ± 1.40
80	65.50 ± 1.46	**68.36 ± 1.26**	63.31 ± 0.49	65.46 ± 0.36	**67.63 ± 0.84**	1.00 ± 0.00	1.00 ± 0.00	10.79 ± 16.96	64.67 ± 0.44	**67.49 ± 0.32**	**67.71 ± 0.50**	63.72 ± 0.74
90	63.92 ± 1.26	**68.48 ± 0.42**	1.00 ± 0.00	1.00 ± 0.00	51.43 ± 2.00	1.00 ± 0.00	1.00 ± 0.00	1.00 ± 0.00	9.38 ± 14.51	1.00 ± 0.00	61.08 ± 2.03	1.00 ± 0.00
95	**60.28 ± 0.49**	1.00 ± 0.00	1.00 ± 0.00	1.00 ± 0.00	1.00 ± 0.00	1.00 ± 0.00	1.00 ± 0.00	1.00 ± 0.00	1.00 ± 0.00	1.00 ± 0.00	1.00 ± 0.00	1.00 ± 0.00
98	**55.46 ± 0.69**	1.00 ± 0.00	1.00 ± 0.00	1.00 ± 0.00	1.00 ± 0.00	1.00 ± 0.00	1.00 ± 0.00	1.00 ± 0.00	1.00 ± 0.00	1.00 ± 0.00	1.00 ± 0.00	1.00 ± 0.00
99	**50.41 ± 0.47**	1.00 ± 0.00	1.00 ± 0.00	1.00 ± 0.00	1.00 ± 0.00	1.00 ± 0.00	1.00 ± 0.00	1.00 ± 0.00	1.00 ± 0.00	1.00 ± 0.00	1.00 ± 0.00	1.00 ± 0.00

Table A15: Performance of different pruning methods for CIFAR-100 on VGG-19 with warmup. Bold and underlined values highlight the top performer. Bold values show methods whose confidence intervals overlap with the best performer.

Sparsity (%)	GN	SNIP	GraSP	SynFlow	FD	FP	FTS	HD	HP	HTS
80	23.60 ± 39.14	**68.86 ± 0.91**	66.59 ± 0.27	1.00 ± 0.00	**39.33 ± 34.18**	**69.39 ± 0.41**	67.86 ± 0.49	**68.00 ± 1.19**	66.04 ± 0.66	**45.56 ± 38.60**
90	**69.32 ± 0.72**	**68.36 ± 1.01**	**43.74 ± 37.01**	1.00 ± 0.00	1.00 ± 0.00	1.00 ± 0.00	**69.05 ± 0.92**	66.94 ± 1.28	67.31 ± 0.75	**68.95 ± 0.65**
95	**68.49 ± 0.58**	**68.23 ± 0.72**	65.87 ± 0.92	1.00 ± 0.00	1.00 ± 0.00	1.00 ± 0.00	**68.11 ± 0.54**	64.62 ± 2.28	**67.39 ± 1.06**	**68.19 ± 0.43**
98	51.50 ± 8.64	23.12 ± 26.58	**64.99 ± 0.18**	1.00 ± 0.00	1.00 ± 0.00	1.00 ± 0.00	1.00 ± 0.00	**65.06 ± 1.14**	**65.41 ± 0.58**	42.73 ± 15.33
99	1.00 ± 0.00	1.00 ± 0.00	38.84 ± 32.86	1.00 ± 0.00	1.00 ± 0.00	1.00 ± 0.00	1.00 ± 0.00	**63.49 ± 0.29**	52.11 ± 5.11	1.00 ± 0.00

The results with VGG-19 on CIFAR-100 exhibit a similar trend to those observed on CIFAR-10. Table A14 shows the occurrence of layer collapse in extreme sparsities when no warmup is applied, leading to a significant drop in accuracy. Introducing a simple warm-up phase effectively resolves this issue, as shown in Table A15, restoring pruning performance across all evaluated criteria.

I. Results TinyImageNet

I.1. ResNet18

Table A16: Performance of different pruning methods for TinyImageNet on ResNet-18 without warmup. Bold and underlined values highlight the top performer. Bold values indicate methods whose confidence intervals overlap with those of the best performer. Baseline accuracy (no pruning): 60.63 $\pm$ 0.12.

Sparsity (%)	Random	Magnitude	GN	SNIP	GraSP	SynFlow	FD	FP	FTS	HD	HP	HTS
10	60.23 ± 0.17	**60.54 ± 0.25**	**60.34 ± 0.14**	**60.83 ± 0.36**	59.23 ± 0.23	**60.28 ± 0.22**	**60.41 ± 0.31**	**60.30 ± 0.23**	**60.58 ± 0.22**	**60.64 ± 0.15**	**60.48 ± 0.43**	**60.66 ± 0.20**
20	**60.45 ± 0.33**	**60.30 ± 0.26**	**60.17 ± 0.21**	**60.48 ± 0.31**	58.68 ± 0.70	59.93 ± 0.17	**60.19 ± 0.38**	**60.58 ± 0.20**	**60.33 ± 0.36**	**60.53 ± 0.24**	**60.37 ± 0.10**	**60.24 ± 0.51**
30	**60.06 ± 0.19**	**59.88 ± 0.31**	**59.97 ± 0.24**	**60.03 ± 0.15**	57.95 ± 0.53	59.65 ± 0.25	59.87 ± 0.17	**60.17 ± 0.12**	**60.14 ± 0.19**	**59.92 ± 0.30**	**60.33 ± 0.25**	**60.00 ± 0.34**
40	**60.21 ± 0.05**	**60.16 ± 0.16**	**59.97 ± 0.25**	**60.00 ± 0.27**	57.77 ± 0.61	**59.79 ± 0.41**	**59.66 ± 0.56**	59.82 ± 0.15	**59.99 ± 0.26**	**60.22 ± 0.03**	**60.15 ± 0.04**	**59.99 ± 0.37**
50	**60.12 ± 0.08**	**59.97 ± 0.40**	**59.86 ± 0.24**	59.73 ± 0.22	57.73 ± 0.19	59.29 ± 0.12	59.78 ± 0.16	59.71 ± 0.12	**59.89 ± 0.38**	**59.87 ± 0.40**	**60.18 ± 0.10**	**60.05 ± 0.19**
60	**59.96 ± 0.34**	**59.82 ± 0.13**	59.17 ± 0.27	59.42 ± 0.14	57.77 ± 0.52	57.86 ± 0.21	58.90 ± 0.71	**59.27 ± 0.43**	59.40 ± 0.21	**59.66 ± 0.33**	**59.64 ± 0.07**	**59.59 ± 0.37**
70	**59.37 ± 0.86**	**59.64 ± 0.15**	58.69 ± 0.23	59.02 ± 0.30	57.21 ± 0.64	0.50 ± 0.00	58.46 ± 0.38	58.86 ± 0.15	59.10 ± 0.16	59.14 ± 0.20	**59.52 ± 0.23**	59.09 ± 0.12
80	58.40 ± 0.11	**59.28 ± 0.42**	57.85 ± 0.21	**58.23 ± 0.70**	56.10 ± 0.27	0.50 ± 0.00	56.95 ± 0.32	57.98 ± 0.09	58.24 ± 0.24	**58.76 ± 0.28**	**58.93 ± 0.24**	58.43 ± 0.16
90	57.16 ± 0.19	54.92 ± 0.15	55.52 ± 0.44	56.57 ± 0.30	54.47 ± 0.32	0.50 ± 0.00	54.77 ± 0.44	55.88 ± 0.30	56.57 ± 0.06	57.19 ± 0.16	**57.83 ± 0.12**	57.04 ± 0.34
95	54.39 ± 0.29	52.30 ± 0.06	51.69 ± 0.41	53.28 ± 0.04	52.37 ± 0.62	0.50 ± 0.00	50.56 ± 0.29	52.90 ± 0.33	53.37 ± 0.15	**54.45 ± 0.52**	**55.37 ± 0.40**	54.27 ± 0.36
98	47.38 ± 0.14	44.89 ± 0.31	44.43 ± 0.65	47.54 ± 0.25	46.38 ± 0.29	0.50 ± 0.00	42.97 ± 0.38	46.62 ± 0.06	47.50 ± 0.43	49.56 ± 0.16	**51.05 ± 0.16**	48.30 ± 0.44
99	39.81 ± 0.66	32.90 ± 0.32	37.61 ± 0.39	41.12 ± 0.23	40.25 ± 0.78	0.50 ± 0.00	36.66 ± 0.24	40.46 ± 0.05	41.40 ± 0.36	44.12 ± 0.20	**44.51 ± 0.08**	41.93 ± 0.72

We tested the TinyImageNet dataset to extend our evaluation with a higher-complexity task. Table A16 and Table A17 show that the metrics based on the Hutchinson approximation demonstrate a clear dominance in a more complex task, HP being the best-performing metric across the sparsity spectrum.

Table A17: Performance of different pruning methods for TinyImageNet on ResNet-18 with warmup. Bold and underlined values highlight the top performer. Bold values indicate methods whose confidence intervals overlap with those of the best performer.

Sparsity (%)	GN	SNIP	GraSP	SynFlow	FD	FP	FTS	HD	HP	HTS
80	57.13 ± 0.30	58.48 ± 0.44	50.99 ± 0.77	0.50 ± 0.00	57.26 ± 0.29	**58.85 ± 0.27**	58.69 ± 0.21	**59.25 ± 0.02**	**59.49 ± 0.39**	**59.28 ± 0.11**
90	53.82 ± 0.76	56.33 ± 0.29	51.16 ± 0.73	0.50 ± 0.00	51.95 ± 1.01	55.50 ± 0.32	56.17 ± 0.30	**58.36 ± 0.45**	**58.50 ± 0.36**	57.58 ± 0.27
95	48.37 ± 0.90	52.28 ± 0.11	49.01 ± 1.02	0.50 ± 0.00	30.99 ± 13.47	50.30 ± 0.55	52.58 ± 0.48	**56.58 ± 0.11**	56.00 ± 0.21	53.95 ± 0.14
98	33.66 ± 4.50	44.98 ± 0.02	41.49 ± 1.10	0.50 ± 0.00	0.50 ± 0.00	44.76 ± 0.49	44.93 ± 0.45	**52.07 ± 0.61**	48.94 ± 0.13	46.92 ± 0.57
99	11.44 ± 8.65	39.67 ± 0.67	34.43 ± 1.94	0.50 ± 0.00	0.50 ± 0.00	34.56 ± 1.48	39.33 ± 0.18	**45.75 ± 0.42**	42.32 ± 0.18	42.02 ± 0.23

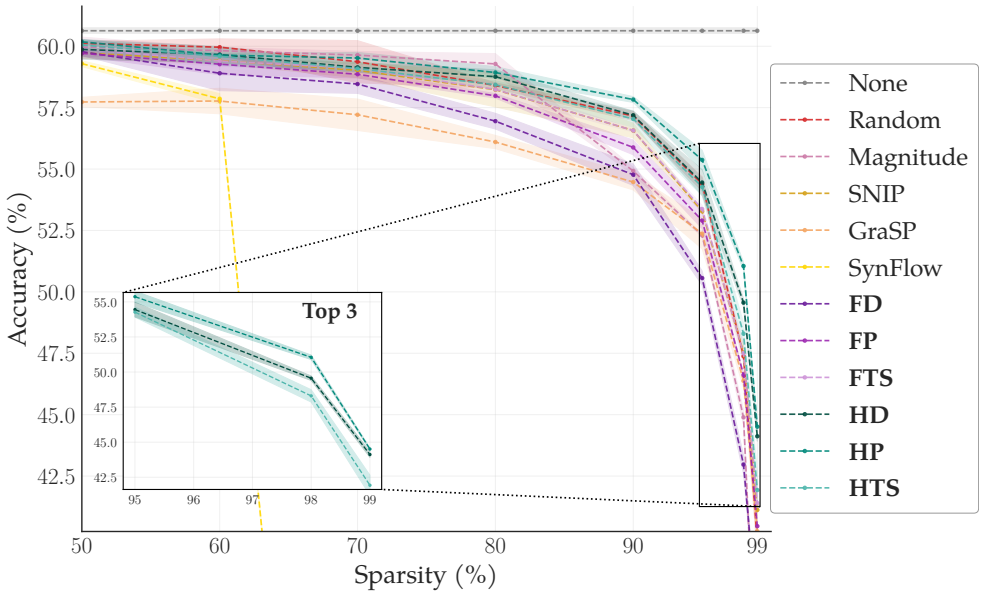

(a) Without warmup

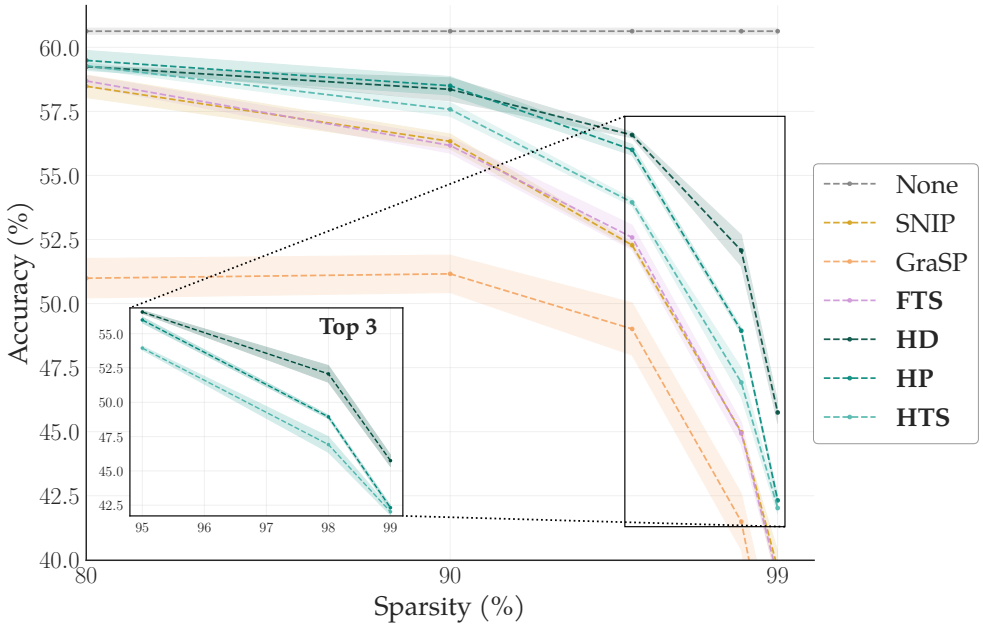

(b) With warmup

Figure A5: Test accuracy for ResNet-18 for the TinyImagenet dataset with and without warmup. For extreme sparsities, we zoom in on the top 3 performers.

J. ImageNet

Table A18: Performance of different pruning methods for ImageNet on ResNet-50. Bold and underlined values highlight the top performer. Bold values indicate methods whose confidence intervals overlap with those of the best performer. Baseline accuracy (no pruning): 73.95 ± 0.18.

Sparsity (%)	Random	Magnitude	SNIP	GraSP	**FTS**	**HD**	**HP**	**HTS**
60	71.61 ± 0.48	**72.70 ± 0.48**	72.03 ± 0.17	70.24 ± 0.21	**72.33 ± 0.40**	**71.76 ± 0.83**	71.08 ± 0.79	72.12 ± 0.09
70	70.25 ± 0.36	**71.47 ± 0.07**	70.69 ± 0.25	68.55 ± 1.26	71.09 ± 0.15	70.91 ± 0.02	70.94 ± 0.17	**71.06 ± 0.47**
80	68.84 ± 0.22	**69.64 ± 0.29**	**69.63 ± 0.23**	67.63 ± 0.52	**69.68 ± 0.15**	68.83 ± 0.12	68.90 ± 0.18	**69.45 ± 0.13**
90	64.21 ± 0.46	63.72 ± 0.43	**65.47 ± 0.50**	62.52 ± 0.50	**65.75 ± 0.04**	**65.08 ± 0.33**	**66.01 ± 0.03**	**66.10 ± 0.85**
95	59.17 ± 0.71	48.08 ± 9.25	61.88 ± 0.36	57.55 ± 1.09	61.50 ± 0.06	59.53 ± 0.26	**60.94 ± 2.05**	**62.87 ± 0.23**
98	49.03 ± 1.12	0.10 ± 0.00	54.36 ± 0.89	50.19 ± 0.72	54.25 ± 1.01	49.71 ± 1.65	**55.55 ± 0.07**	**56.09 ± 0.73**
99	38.64 ± 0.63	0.10 ± 0.00	47.38 ± 0.06	42.07 ± 3.93	**47.47 ± 1.03**	32.79 ± 3.32	**48.49 ± 0.50**	**48.29 ± 1.68**

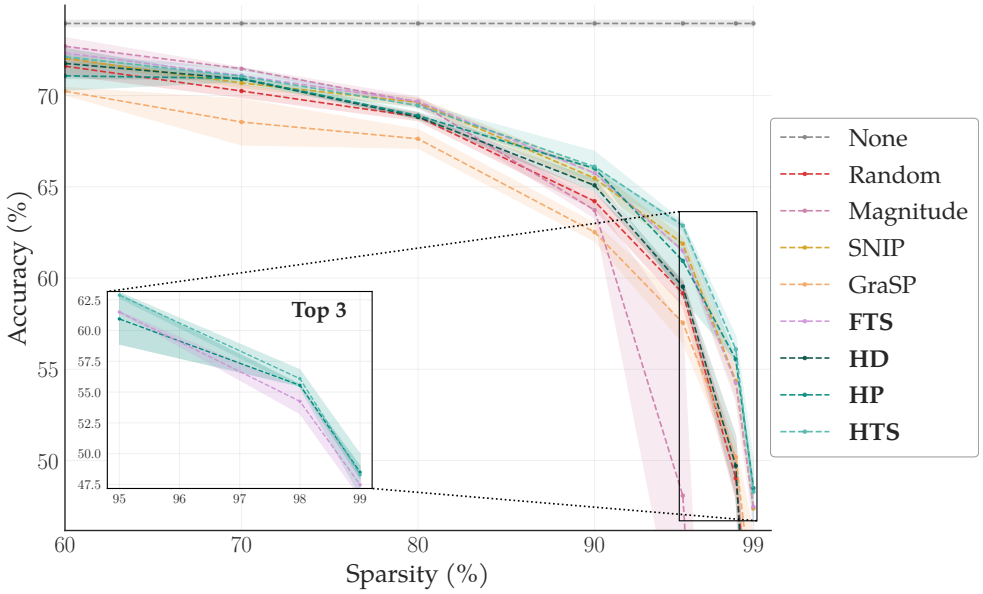

Figure A6: Test accuracy for ResNet-50 for the Imagenet-1k dataset only without warmup. For extreme sparsities, we zoom in on the top 3 performers.

K. Prune After Training CIFAR-10

K.1. ResNet18

Table A19: Performance of different pruning methods for CIFAR-10 on ResNet-18 (PaT). Bold and underlined values highlight the top performer. Bold values show methods whose confidence intervals overlap with the best performer. Baseline accuracy (no pruning): 93.73 $\pm$ 0.20.

Sparsity (%)	Random	Magnitude	GN	SNIP	GraSP	SynFlow	FD	FP	FTS	HD	HP	HTS
10	93.60 ± 0.06	**93.84 ± 0.06**	**93.76 ± 0.13**	**93.80 ± 0.08**	92.76 ± 0.05	**93.88 ± 0.11**	**93.83 ± 0.16**	**93.80 ± 0.04**	**93.78 ± 0.07**	**93.86 ± 0.11**	**93.92 ± 0.08**	**93.77 ± 0.11**
20	**93.60 ± 0.15**	**93.83 ± 0.06**	**93.83 ± 0.09**	**93.80 ± 0.06**	91.85 ± 0.17	**93.79 ± 0.14**	**93.76 ± 0.10**	**93.85 ± 0.07**	**93.83 ± 0.07**	**93.88 ± 0.24**	**93.83 ± 0.09**	**93.79 ± 0.10**
30	93.61 ± 0.09	**93.82 ± 0.07**	**93.83 ± 0.16**	**93.81 ± 0.05**	91.69 ± 0.50	93.49 ± 0.04	**93.76 ± 0.11**	**93.79 ± 0.07**	**93.79 ± 0.06**	**93.63 ± 0.16**	**93.88 ± 0.15**	**93.77 ± 0.05**
40	93.39 ± 0.20	**93.84 ± 0.06**	**93.79 ± 0.14**	**93.76 ± 0.05**	91.83 ± 0.40	93.49 ± 0.08	**93.75 ± 0.10**	**93.77 ± 0.05**	**93.83 ± 0.04**	**93.74 ± 0.15**	**93.79 ± 0.17**	**93.81 ± 0.05**
50	93.44 ± 0.20	**93.86 ± 0.08**	**93.77 ± 0.08**	**93.74 ± 0.05**	91.47 ± 0.28	93.54 ± 0.14	93.60 ± 0.06	**93.71 ± 0.12**	**93.77 ± 0.10**	93.59 ± 0.18	93.58 ± 0.01	**93.71 ± 0.15**
60	93.19 ± 0.06	**93.83 ± 0.09**	**93.84 ± 0.12**	**93.71 ± 0.13**	91.34 ± 0.24	**93.56 ± 0.21**	**93.84 ± 0.08**	**93.68 ± 0.07**	**93.75 ± 0.04**	**93.88 ± 0.18**	**93.61 ± 0.09**	93.59 ± 0.10
70	92.85 ± 0.27	**93.80 ± 0.04**	**93.69 ± 0.12**	93.49 ± 0.14	91.19 ± 0.10	10.00 ± 0.00	**93.74 ± 0.14**	93.50 ± 0.03	93.57 ± 0.09	**93.69 ± 0.09**	93.60 ± 0.15	93.49 ± 0.06
80	91.07 ± 0.35	93.55 ± 0.07	93.60 ± 0.04	**93.55 ± 0.21**	91.29 ± 0.21	10.00 ± 0.00	**93.58 ± 0.17**	**93.67 ± 0.07**	**93.50 ± 0.19**	93.43 ± 0.13	**93.72 ± 0.06**	**93.60 ± 0.19**
90	89.12 ± 0.30	92.95 ± 0.12	**93.36 ± 0.20**	**93.30 ± 0.10**	90.55 ± 0.39	10.00 ± 0.00	**93.39 ± 0.15**	**93.32 ± 0.18**	**93.18 ± 0.26**	92.90 ± 0.26	**93.37 ± 0.30**	**93.25 ± 0.16**
95	87.53 ± 0.29	92.29 ± 0.11	92.36 ± 0.14	**92.56 ± 0.19**	89.95 ± 0.38	10.00 ± 0.00	92.19 ± 0.27	**92.50 ± 0.17**	**92.69 ± 0.21**	92.13 ± 0.24	**92.70 ± 0.07**	**92.56 ± 0.28**
98	84.45 ± 0.37	90.91 ± 0.17	90.46 ± 0.17	90.84 ± 0.30	88.46 ± 0.66	10.00 ± 0.00	90.14 ± 0.23	91.16 ± 0.15	91.07 ± 0.21	90.16 ± 0.07	**91.41 ± 0.02**	90.81 ± 0.22
99	81.01 ± 0.36	**89.30 ± 0.52**	88.70 ± 0.17	**89.01 ± 0.55**	87.19 ± 0.14	10.00 ± 0.00	87.85 ± 0.29	**89.10 ± 0.33**	**89.10 ± 0.27**	88.69 ± 0.42	**89.52 ± 0.25**	88.87 ± 0.35

Table A20: Performance delta (PaT - PaI with warmup) for CIFAR-10 on ResNet-18. Positive values indicate PaT performs better, negative values indicate PaI performs better.

Sparsity (%)	Random	Magnitude	GN	SNIP	GraSP	SynFlow	FD	FP	FTS	HD	HP	HTS
80	-1.57 ± 0.35	0.20 ± 0.07	0.28 ± 0.04	0.25 ± 0.21	-0.44 ± 0.21	0.00 ± 0.00	0.06 ± 0.17	0.31 ± 0.07	0.03 ± 0.19	0.15 ± 0.13	0.40 ± 0.06	0.08 ± 0.19
90	-2.26 ± 0.30	0.09 ± 0.12	0.65 ± 0.20	0.18 ± 0.10	-1.04 ± 0.39	0.00 ± 0.00	0.50 ± 0.15	0.23 ± 0.18	0.18 ± 0.26	0.26 ± 0.26	0.50 ± 0.30	0.10 ± 0.16
95	-2.06 ± 0.29	0.24 ± 0.11	0.20 ± 0.14	0.24 ± 0.19	-0.94 ± 0.38	0.00 ± 0.00	12.61 ± 0.27	0.98 ± 0.17	0.42 ± 0.21	-0.07 ± 0.24	0.52 ± 0.07	0.33 ± 0.28
98	-1.84 ± 0.37	2.46 ± 0.17	0.18 ± 0.17	0.55 ± 0.30	-1.32 ± 0.66	0.00 ± 0.00	80.14 ± 0.23	1.85 ± 0.15	0.80 ± 0.21	-1.08 ± 0.07	0.86 ± 0.02	0.56 ± 0.22
99	-1.91 ± 0.36	12.76 ± 0.52	28.63 ± 0.17	0.65 ± 0.55	-0.79 ± 0.14	0.00 ± 0.00	77.85 ± 0.29	3.71 ± 0.33	1.08 ± 0.27	-0.78 ± 0.42	0.73 ± 0.25	0.81 ± 0.35

Frankle et al. [27] previously criticized PaI methods for consistently underperforming compared to magnitude PaT. However, their analysis did not assess how the PaI-designed criteria perform in the PaT setting. Table A19 shows that second-order-based criteria remain top performers across sparsities in the PaT setting. Table A20 presents the test accuracy delta between PaI and PaT settings. As we increase sparsity, it is clear that the advantage of magnitude PaT comes at the expense of training a fully dense model and the retraining required.

L. Pre-Finetune Pruning for Transformers

Training Setup. All models were fine-tuned using the same training protocol and hyperparameters. As transformers are known to be data-hungry, we pruned the default initialization in Torch (from ImageNet-1K) before fine-tuning for 30 epochs, similar to the approach in [46]. As sparsity increases, the model's size and FLOPs are drastically reduced. We emphasize that our goal in this experiment is not to optimize transformer compression performance, but to assess whether pruning-at-initialization metrics, originally designed for unstructured pruning, remain informative when applied to structured pruning decisions in transformer architectures, something demonstrated in [48].

Table A21: Summary results of structured pruning: we used different criteria to perform per-layer pruning for the model ViT-B/16 in the CIFAR-10 dataset. Bold values indicate the best average performance among three random seeds. Baseline accuracy (no pruning): 85.78 ± 1.56.

Sparsity (%)	FLOPs	Runtime (min)	Random	Magnitude	SNIP	GraSP	FD	FP	FTS	HD	HP	HTS
20	4.49G	55	85.75 ± 0.20	85.79 ± 0.36	**86.34 ± 0.44**	84.86 ± 0.52	86.07 ± 0.86	85.63 ± 0.66	85.77 ± 0.38	85.21 ± 0.64	85.28 ± 0.60	86.01 ± 0.48
36	3.59G	44	85.18 ± 0.28	84.84 ± 0.46	85.43 ± 0.39	83.42 ± 1.81	85.31 ± 0.16	85.15 ± 0.45	**85.45 ± 0.24**	84.96 ± 0.65	84.99 ± 0.04	85.21 ± 0.42
52	2.69G	38	83.75 ± 0.56	83.91 ± 0.09	83.82 ± 0.21	82.62 ± 0.79	83.88 ± 0.14	83.58 ± 0.57	83.83 ± 0.47	83.73 ± 1.16	83.75 ± 0.48	**84.37 ± 0.28**
64	2.02G	29	83.31 ± 0.45	82.95 ± 0.29	82.91 ± 0.62	82.19 ± 0.59	82.75 ± 0.17	83.26 ± 0.10	82.80 ± 0.21	82.32 ± 1.67	83.02 ± 0.25	**83.60 ± 0.35**
75	1.40G	22	82.07 ± 0.50	**82.29 ± 0.61**	81.89 ± 0.57	81.44 ± 0.35	81.86 ± 0.17	81.64 ± 0.73	81.70 ± 0.59	82.07 ± 1.05	81.95 ± 0.51	81.88 ± 0.65
84	0.90G	18	76.79 ± 0.32	74.31 ± 1.28	**79.34 ± 0.55**	76.10 ± 2.20	78.87 ± 0.56	78.67 ± 0.42	79.15 ± 0.24	78.76 ± 0.43	78.41 ± 0.20	78.71 ± 0.80
91	0.50G	13	75.18 ± 0.69	69.23 ± 0.91	77.20 ± 0.73	76.05 ± 0.37	77.31 ± 0.67	76.37 ± 0.95	77.10 ± 0.89	76.78 ± 0.99	76.69 ± 0.70	**77.62 ± 0.73**
99	0.06G	10	72.57 ± 0.08	69.79 ± 1.14	73.00 ± 0.57	73.42 ± 0.62	73.28 ± 0.24	73.47 ± 0.97	73.32 ± 0.74	72.90 ± 1.24	73.18 ± 0.82	**73.48 ± 1.39**

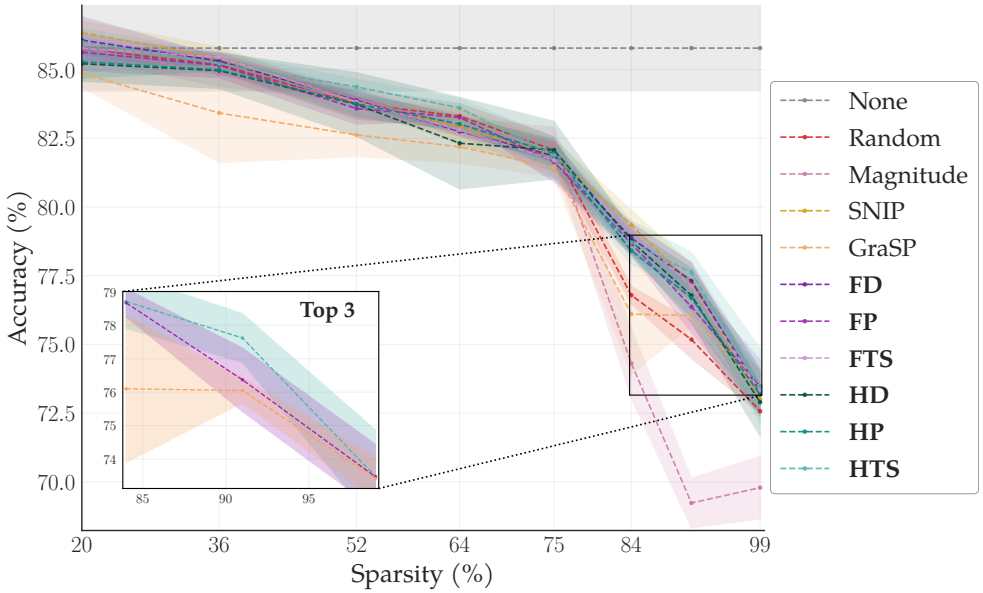

Figure A7: Structured pruning of ViT-B/16 in CIFAR-10: Test accuracy across sparsities for all the importance-based metrics.

M. Comparison of our criteria with magnitude-based pruning

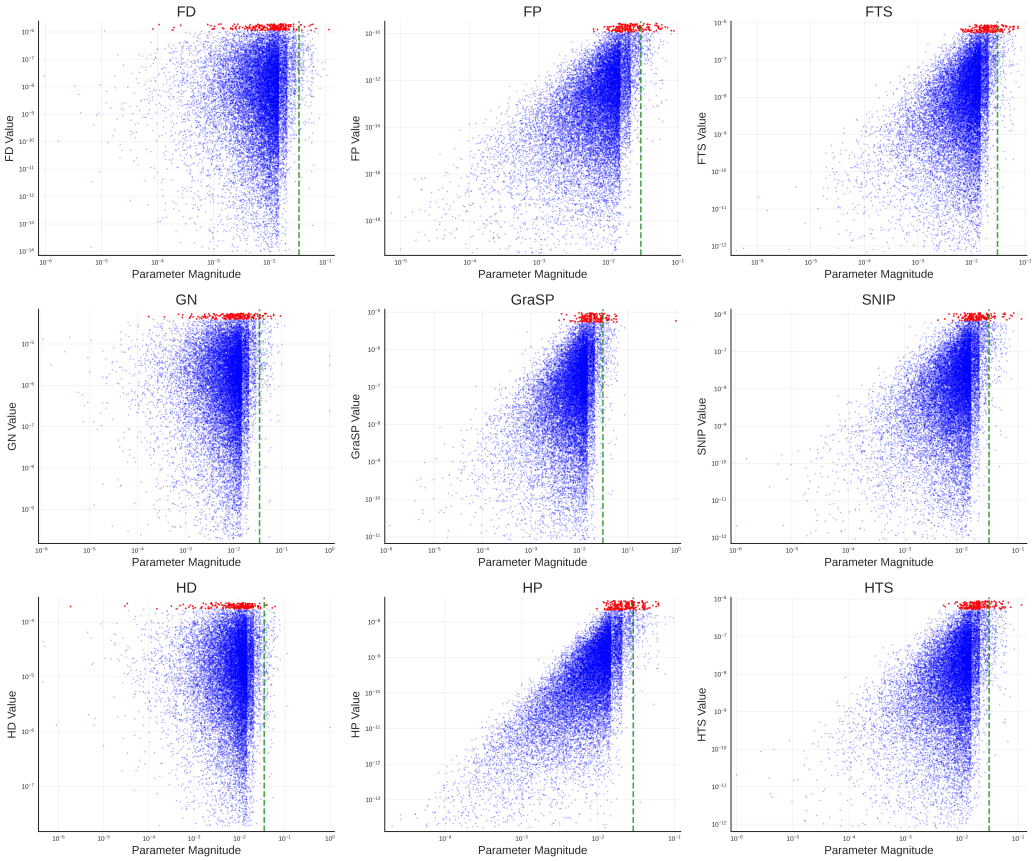

Figure A8: Proposed criteria vs. Magnitude parameter selection for 99% sparsity (ResNet18, CIFAR-10, Seed 0)

Figure A8 illustrates the relationship between parameter magnitude and different sensitivity-based pruning metrics. Each point represents a model parameter, with red points indicating the top-1% parameters selected for retention by each criterion. The green dashed line marks the 99th percentile of parameter magnitudes. A key observation is that the success of data-based methods relies on the ability to consider small-magnitude parameters that magnitude-based pruning discards.